People`s Democratic Republic of Algeria
Ministry of Higher Education and Scientific Research
University of Echahid Hamma Lakhdar - El Oued
Faculty of Technology
Department of Electrical Engineering
Dissertation
ACADEMIC MASTER
Domain: Science and Technology
Division: Electrotechnical
Specialty: Electric Control

Presented by:

- **Dadda Taki Eddine**
- **Guemari Ilyas**

Entitled:

High-Speed Sensorless Control for Induction Motor Drives

Dissertation Submitted in Partial Fulfillment of the Requirements for the Master
Degree in Electric Control
Publicly defended on: 05 / 06 / 2024

Board of Examiners:

Dr. Chouaib Labiod	**Chairman**
Prof. Zoheir TIR	**Supervisor**
Dr. Cherifa Hakima	**Examiner**

Thesis prepared within the Laboratory of Exploitation and Valorization of Saharan Energy Resources
Academic Year: 2023/2024

Dedication

We extend our deepest gratitude to the Almighty Allah for granting us the strength and resilience required to achieve our goals.

We sincerely appreciate the exceptional individuals whose significant contributions have aided us in reaching our objectives.

To our beloved parents, whose enduring love, unwavering support, and confidence in our abilities have been a constant source of inspiration.

To our esteemed supervisor, whose invaluable guidance, continuous encouragement, and approachability have played a pivotal role in our success.

We also express heartfelt thanks to our extended family members and close friends for their unwavering support and constant encouragement.

Lastly, we convey our profound appreciation to all our esteemed professors for their invaluable mentorship, unwavering guidance, and extensive knowledge imparted during our academic journey.

Acknowledgments

The culmination of this research owes its realization to the collaboration of various individuals, whose identities remain undisclosed herein. Our sincere appreciation extends to Professor Zoheir TIR, our supervisor, for his unwavering support and invaluable guidance throughout this endeavor. Additionally, we recognize the administrative personnel for their assistance and express gratitude to our educators for their insightful direction. Moreover, we are indebted to the LEVRES laboratory for their hospitality and provision of essential resources crucial to the fruition of this project. Nevertheless, any inaccuracies or oversights within this dissertation are attributed solely to the authors.

Contents

Table of figures

Nomenclature

$1, \overline{a}, \overline{a^2}$	unity vectors
$Angle$	stator flux position compensator output
B	friction constant
C_{dc}	dc link capacitance
C	constant value resulting from initial conditions of the integral
D_A, D_B, D_C	switching states of inverter legs
$D_{1..6}$	diodes to protect switches of the inverter (from1to 6)
e	back electromotive force
f_c	cut-off frequency (Hz)
f_{fund}	fundamental frequency
f_{pwm}	switching frequency
fs	sampling frequency
f_{stN}	nominal stator frequency
$Gain$	stator flux gain compensator output
$G_{(plant)}$	transfer function of the plant
$G_{(ol)}$	open loop transfer function
$G_{(cl)}$	close loop transfer function
i_s	stator current
i_{sN}	nominal stator current
J	inertia
j	imaginary unit
$k_A(t), k_B(t), k_C(t)$	arbitrary phase quantities in the natural coordinates (A, B, C)
K_p, K_i	proportional and integral PI ragulator gains, respectively
K_a	antiwindup gain
L_s, L_r, L_m	stator, rotor and magnetizing inductances, respectively
L_s'	transient inductance
l_σ	equivalent inductance: $L_\sigma = L_r L_s - {L_m}^2$
L_1, L_2, L_3	three phases
T_e	electromagnetic torque
T_{eN}	nominal electromagnetic torque
T_l	load torque
T_k	breakdown torque
M_p	maximum overshoot
n_r	rotor rotational speed
n_e	synchronous rotational speed
p_p	number of pole pairs
p	Laplace operator
p_{pol}, q_{pol}	degrees of numerator and denominator polynomials, respectively

R_s, R_r	stator and rotor resistances, respectively
s	slip
$T_{1..6}$	switches of the inverter (from 1 to 6)
T_d	time delay of the transportation lag
T_{pwm}	switching time period
T_s	sampling time
T_{sim}	simulation time
T_s'	time constant of the plant in d current control loop
T_ψ	time constant of the plant in the flux control loop
T_σ	one of the time constants of the plant in flux control loop: $T_\sigma = L_\sigma/(R_r L_s)$
T_r	rotor time constant
T_{st}	stator time constant
T_{ol}^{eq}	equivalent time constant of the open loop system
T^{eq}	equivalent time constant of the control loop
$t_{r(10\%-90\%)}$	rising time
$t_{s(2\%)}$	settling time
U_{dc}	dc link voltage
u_s	stator voltage
u_A, u_B, u_C	phase voltages
u_{AB}, u_{BC}, u_{CA}	line to line voltages
u_N	nominal voltag
u_{RMS}	RMS voltage
$u_{S\psi}$	voltage placed after the stator resistance, in the typical equivalent circuit of ind. motor
X_s, X_r, X_m	stator, rotor and magnetizing reactances, respectively
X	input to high pass filter in the flux observer structure
Y	output of high pass filter in the flux observer structure
Z	output of the pure integrator in the flux observer structure
z	discrete domain operator
ψ_s	stator flux
ψ_{s0}	compensated stator flux
ψ_{sN}	nominal stator flux
$\psi_{s(mach)}$	stator flux generated inside the machine (simulation case)
ψ_r	rotor flux
θ_e	angle of the stator flux
θ_{e0}	compensated angle of the stator flux
$\theta_{e(mach)}$	angle of the stator flux generated in the motor (simulation case)
θ_x, θ_y	angle of back EMF, before and after HPF, respectively
ω_e	synchronous angular speed
ω_r	rotor angular speed

ω_r^{el}	electrical angular rotor speed
ω_{sl}	slip angular speed
ω_{slk}	breakdown slip angular speed
ω_{slN}	nominal slip angular speed
ω_c	cut off frequency (rad/s)
$\hat{x}$	magnitude of the variable
$\overline{x}$	vector representation of the variable
x^s	variable represented in stationary reference frame
x^e	variable represented in synchronously rotating reference frame
x_d, x_q	real and imaginary components of the variable, respectively
$x_{i_{sd}}$	variable of the d current control loop
x_ψ	variable of the flux control loop
$x_{i_{sq}}$	variable of the q current control loop
x_ω	variable of the speed control loop
x_{off}	offset value of the measured variable
x^*	estimation of the variable
x_{conj}	conjugated complex number
$x_{(ref)}$	reference value of the variable
$x_{(err)}$	error of the variable
$x_{(meas)}$	measurement of the variable
$\Im$	indicates imaginary part of the complex number
σ	total leakage factor
γ_m	angle of the actual rotor displacement
τ	integral time constant of PI regulator
ζ	damping ratio

Abbreviations

AC - Alternating Current
AAIA - Accurate Adaptive Integration Algorithm
CSI - Current Source Inverter
DC - Direct Current
DSP - Digital Signal Processor (Processing)
DTC - Direct Torque Control
EMF - Electromotive Force
FOC - Field Oriented Control
HPF - High-Pass Filter
IM - Induction Motor (Machine)
LPF - Low-Pass Filter
MFOC - Magnetising Field Oriented Control
PCB - Printed Circuit Board
PMSM - Permanent Magnet Synchronous Motor(Machine)
PWM - Pulse-Width Modulation
RFOC - Rotor Field Oriented Control
RTI - Real Time Implementation
SFOC - Stator Field Oriented Control
SVM - Space Vector Modulation
VSC - Voltage Source Converter
VSI - Voltage Source Inverter

Summary

The project aims to design a sensorless stator field-oriented control algorithm for high-speed drives. However, due to the unavailability of such motors in the university laboratories, a conventional motor with a rated frequency of 50 Hz is utilized. The project is structured into several key subtasks.

The introductory chapter provides a comprehensive background, highlighting the advantages, applications, and types of high-speed drives. It offers a comparative analysis of the two primary motor types used in these applications. This chapter also reviews various control methods for high-speed drives and addresses specific challenges and their solutions, thereby delineating the project's scope and limitations.

Chapter two is dedicated to the mathematical modeling of the drive system. It begins with the necessary assumptions and proceeds with a formal system description. The mathematical model is constructed and validated using the basic V/f control approach.

The detailed design process starts with the fundamental principles of field-oriented control, with a particular emphasis on stator field-oriented control. Subsequent sections delve into the design of the control strategy, including the development of a sensorless control algorithm, flux observer, and speed estimator. The proposed algorithm is rigorously tested and validated through simulation results.

Overall, this project systematically addresses the development and validation of a sensorless stator field-oriented control algorithm, providing significant insights into its application for high-speed drives.

Keywords: Induction motor (IM), Stator Vector control, flux observe

ملخص

يهدف المشروع إلى تصميم خوارزمية تحكم موجهة للمجال بدون مستشعر للمحركات ذات السرعات العالية. ومع ذلك، نظرًا لعدم توفر مثل هذه المحركات في مختبرات الجامعة، يتم استخدام محرك تقليدي بتردد مقنن قدره 50 هرتز. يتم هيكلة المشروع إلى عدة مهام رئيسية.

يوفر الفصل التمهيدي خلفية شاملة، تسلط الضوء على مزايا وتطبيقات وأنواع المحركات ذات السرعات العالية. يقدم تحليلًا مقارنًا لنوعي المحركات الأساسيين المستخدمين في هذه التطبيقات. كما يستعرض هذا الفصل مختلف طرق التحكم في المحركات ذات السرعات العالية ويعالج التحديات الخاصة وحلولها، مما يحدد نطاق المشروع وحدوده.

يُخصص الفصل الثاني للنمذجة الرياضية لنظام القيادة. يبدأ بالافتراضات اللازمة ويستمر بوصف النظام بشكل رسمي. يتم بناء النموذج الرياضي والتحقق من صحته باستخدام نهج التحكم الأساسي.V/f

تبدأ عملية التصميم التفصيلية بالمبادئ الأساسية للتحكم الموجه للمجال، مع التركيز بشكل خاص على التحكم الموجه للمجال الساكن. تتناول الأقسام اللاحقة تصميم استراتيجية التحكم، بما في ذلك تطوير خوارزمية التحكم بدون مستشعر، ومراقب التدفق، ومقدر السرعة. يتم اختبار الخوارزمية المقترحة والتحقق من صحتها من خلال نتائج المحاكاة.

بشكل عام، يعالج هذا المشروع بشكل منهجي تطوير والتحقق من صحة خوارزمية التحكم الموجهة للمجال الساكن بدون مستشعر، مما يوفر رؤى هامة حول تطبيقها في المحركات ذات السرعات العالية.

الكلمات المفتاحية: المحرك الحثي ، التحكم الشعاعي للمجال الساكن، مراقب التدفق

r

1 Introduction

The first chapter of the report provides the essential information required for subsequent research and analysis. It begins with a brief overview of the advantages of high-speed drives and their applications. As these drives predominantly use two types of motors, a proper comparison between them is presented. Following this, a review of the methods used to control high-speed drives is conducted. To fully leverage the benefits of high-speed drives, specific problems and challenges that need to be addressed are discussed. This completes the presentation of high-speed systems. Subsequently, the exact scope and limitations of the project are outlined. The chapter concludes with the structure of the report.

1.1. High speed drives applications

Recently, high-frequency drives have garnered increased interest within the industry. This interest is primarily driven by the numerous advantages these types of drives offer. Generally, increased speed enhances efficiency, thereby improving the operation of various applications. Additionally, the reduction in weight and size is achieved without compromising output power. Lower mass results in lower rotor inertia, which contributes to better dynamic responses. These benefits are evident in applications such as micro-turbine generators, centrifugal compressors, pumps, gas turbine drives, and machine tool spindles [1]-[2], [3]. Furthermore, high-speed drives are frequently used in applications involving PCB drilling machines [4] and in the wood industry [5]. Both environments demand fast processing and improved product quality.

In the case of PCB drilling machines, there is a technological competition between laser drilling and mechanical drilling. With the continuous increase in the speed of drillers, which are available in the market with speeds ranging from 30,000 rpm to 200,000 rpm [4], and the reduction in drilling diameters, it appears that mechanical solutions can achieve more accurate results. Successful tests have been conducted at speeds up to 300,000 rpm [4].

Woodworking machinery is another area where high-frequency drives are extensively used. The primary reason for their usage is the lack of mechanical gear, which results in reduced maintenance frequency, increased efficiency (due to fewer mechanical losses), and more flexible operation. The ability to fit the output frequency of the inverter with the required speed of the chosen tool is particularly advantageous. Moreover, during non-operational times, the machine can be powered down, saving energy and reducing noise. If a specific tool is needed, it can be easily accelerated to the required working speed. Two types of high-speed drives are commonly used: one with a gearbox and the other utilizing frequency control.[6]

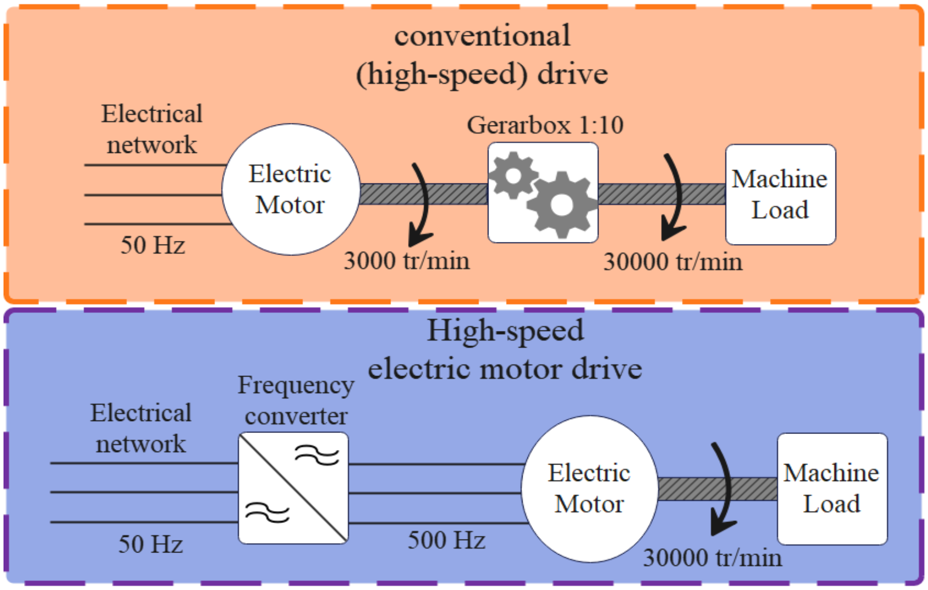

Figure 1. 1: Comparison between conventional high-speed drives, consisting of a gearbox, and one using inverter. [3]

1.1. Induction Motor vs PM Synchronous Motor

In high-speed drives, two primary types of motors are commonly employed: induction motors (IM) and permanent magnet synchronous motors (PMSM). Each motor has its own advantages and drawbacks, which need to be carefully considered. This comparison is based on the discussion presented in [7].

From a thermal and mechanical perspective, induction motors are highly robust, ensuring operation in high temperatures. This robustness is crucial at higher speeds, where temperature increases due to factors such as eddy currents, which are speed-dependent. Conversely, PMSMs have a limited temperature range due to the sensitivity of permanent magnet materials to heat, restricting their high-speed capabilities.

Electrically, PMSMs offer superior performance due to the presence of permanent magnet materials mounted on the rotor. These motors provide a higher power factor and greater electrical efficiency. This results in a high power per volume ratio. However, IMs exhibit relatively high rotor losses due to circulating currents in the rotor bars. To mitigate higher harmonics in the air gap (which cause additional losses) and to improve cooling, the air gap size in IMs is extended. This leads to large resistive losses in the stator windings and a low power factor.

It is also noteworthy that PMSMs delivering the same amount of power as their IM counterparts are considerably smaller. Moreover, PMSMs do not have the mechanical issues associated with the larger rotor sizes of IMs, making them robust and sturdy.

When comparing costs, constructing an induction machine is generally cheaper due to the lower cost of materials. However, to achieve the same output power, an induction machine must be larger than a PMSM, which increases the overall cost. In the case of PMSMs, the main cost driver is the permanent magnet materials. Despite this, the final motor size is smaller, and the materials needed are reduced. Additionally, PMSMs require smaller and cheaper frequency converters, enhancing their cost-efficiency.

Therefore, the overall cost of an effective drive system tends to be lower for synchronous machines.

The advantages and disadvantages of both motor types are summarized in Table 1.1. Based on the discussed aspects, it can be concluded that induction motors are capable of operating at higher power in a larger speed range, while permanent magnet synchronous machines offer better efficiency but are limited in speed. It is clear that PMSMs provide better solutions within a similar IM drive range. However, due to the speed limitations of PMSMs, IMs are considered for broader applications. For the scope of this project, the focus is placed on the induction motor.

	INDUCTION MOTOR	PM SYNCHRONOUS MOTOR
OPERATION IN HIGHER TEMPERATURE	possible	limited
MECHANICAL SIZE	bigger	smaller
POWER FACTOR	lower	bigger
EFFICIENCY	lower	bigger
MACHINE COST	comparable	
DRIVE COST	higher	lower

Table 1.1: Summarized comparison between Induction Motor and Permanent Magnet Synchronous Motor used in high-speed applications.

1.3 Control techniques

High-speed drives remain a largely unexplored field, with limited existing literature. Consequently, references focusing on Permanent Magnet Synchronous Motors (PMSM) are also included in the research.

The initial description highlights the benefits of high-speed drives, emphasizing the need for stable and efficient control. Most proposed algorithms are based on vector control. Simple open-loop scalar control was also tested with satisfactory results, achieving speeds up to 100,000 rpm [8]. This indicates that V/f control is an appealing solution due to its simplicity and the absence of a mechanical sensor for rotor position measurement. Despite this, it heavily relies on machine parameters, which cannot be compensated for due to the lack of feedback signals. This results in a time-consuming process for proper implementation and adjustment.

A control scheme gaining more interest in low and medium speed applications is Direct Torque Control (DTC). DTC ensures instantaneous control of torque and flux. However, in high-speed cases, realizing DTC becomes very challenging due to the need for a high sampling rate, which is difficult to achieve at high velocities [2].

The drawbacks of scalar control and DTC extend the scope to Field Oriented Control (FOC). It has been observed that FOC, particularly in high-speed applications, yields very good results. FOC can be categorized into two groups: Rotor Field Oriented Control (RFOC) [1], [8], [2], [9], and Stator Field Oriented Control (SFOC) [4],[10]

Due to PMSM's better performance, many authors have attempted to implement control on this machine type. Bon-Ho Bae et al. [1] proposed the RFOC method to overcome challenges such as low stator inductance and high DC-link voltage. Their tests compared vector control with scalar control, showing better performance with RFOC. They suggested using a self-tuning flux observer to address speed estimation and position issues and developed a robust speed estimator. Similar challenges, including the back electromotive force (EMF) issue at low speeds, were addressed by Longya Xu and Changjiang Wang [8]. Future research aims at achieving speeds of 100,000 rpm and higher.

Significant research by Ralph M. Kennel [4]. examined sensorless field-oriented control for machines with speeds up to 300,000 rpm. In high-speed scenarios, mechanical movement of the rotor for 1° can last 555 ns. To meet these demands, a microprocessor is necessary. SFOC was proposed with hardware-based solutions, focusing on reaching velocities of 600,000 rpm.

Another approach to sensorless control was discussed by R. Bojoi et al. [10] , who focused on low-cost applications with high torque abilities. Their work highlighted the need to decouple torque and flux commands, avoiding feedback signals for i_d current, thus simplifying the system

This analysis concludes that sensorless strategies should be further explored in algorithm design. SFOC and RFOC must be compared to determine the best-fit option for each project [11].. Further studies will begin with SFOC, assuming a linear relationship between control variables $\left(i_{sd}, i_{sq}\right)$ and the output value (torque). Simple rotor voltage equations are used to employ a current-controlled PWM inverter, simplifying the process. The formula for calculating flux in rotor field coordinates depends on machine parameters $(R_s, \sigma X_s)$:

$$\overline{\psi}_r = \frac{X_r}{X_m}\left[\int \left(\overline{u}_s - R_s \cdot \overline{i}_s\right)dt - \sigma X_s \overline{i}_s\right] \tag{1.1}$$

where:

- $\overline{\psi}_r$ is rotor flux (in vector representation),
- $\overline{u}_s$and $\overline{i}_s$ are stator voltage and current, respectively (in vector representation),
- R_s is stator resistance,
- X_s, X_r, X_m are stator, rotor, and magnetizing reactances, respectively,
- σ is the total leakage factor.

In the stator field-oriented control case, coupling between controlled variables and output must be compensated. This complexity makes rotor voltage equation implementation with a current-controlled inverter challenging. SFOC, however, provides an easier decoupling process and a simple expression for stator flux, dependent only on R_s:

$$\overline{\psi}_s = \int \left(\overline{u}_s - R_s . \overline{i}_s\right)dt \tag{1.2}$$

where,

$\overline{\psi}_s$ is a stator flux (in vector representation).

Summarizing, the ease of working with voltage source converters (VSC) and a simple formula for flux calculation are crucial in vector control, making SFOC the preferred method for further analysis. Thus, sensorless field-oriented control is chosen for detailed study.

1.4 Challenges and problems

Despite the advantages of high-speed drive applications, several challenges and issues need to be addressed. As previously mentioned, one critical aspect is obtaining reliable position (or speed) information. Commonly used mechanical sensors mounted on the shaft often prove unreliable. At high rotational speeds, they fail to provide accurate measurements and sufficient resolution (e.g., angle information from Hall-effect sensors has a resolution of ±30°) [1]. Additionally, installing and maintaining these sensors is difficult, limiting mechanical design and causing aerodynamic issues [1]. An alternative solution is sensorless control, which overcomes these difficulties and significantly reduces drive costs [8].

A crucial issue is the need for fast computation control strategies to achieve real-time control [8]. This necessitates the use of high-speed digital signal processors. Sometimes, employing any kind of DSP is impossible because they may not be fast enough for the required calculations. In ultra-high-speed scenarios, control algorithms are executed by hardware [4].

Choosing the proper power converter is essential. It must operate with a high switching frequency, adhering to the relationship [8]:

$$\frac{f_{pwm}}{f_{fund}} \geq 10 \tag{1.3}$$

where:

f_{PWM} is the switching frequency,

f_{fund} is the fundamental frequency.

The converter must also resist high switching frequency losses during operation at high frequencies.

Analyzing existing problems necessitates considering non-linear effects like dead-time or zero-current slumping effects [1]. These can degrade the current wave, causing additional system losses. High-speed drives introduce extra heat sources compared to conventional drives operating at 50Hz. As rotational speed increases, so do eddy current losses and friction losses (dependent on the square and cubic of speed, respectively) [3]. Proper compensation for these effects is crucial to reduce losses.

Another speed-related challenge is back electromotive force (EMF). Its increase causes a reduction in supply voltage. The maximum produced electromagnetic torque is proportional to the square of that voltage. Consequently, torque reduces rapidly with decreasing voltage. Thus, to achieve maximum torque at high speeds, field-weakening algorithms are necessary [8], [10].

Similar to normal drives (supplied at 50Hz), high-speed drives face variations in parameters due to phenomena like temperature rise, skin effect, or saturation. In high-speed applications, this variability is amplified. This requires careful consideration in the design of regulators to ensure proper control.

Additional issues include significant stress on the stator winding insulation or bearing currents. To mitigate these, using current source inverters (CSI) instead of traditional voltage source inverters (VSI) is recommended [11].

To summarize, high-frequency drives, despite their advantages, present several problems and challenges that must be addressed to ensure reliable operation. The following sections will outline the project's objectives and review solutions to maintain system functionality.

1.5 Objectives and limitations

In the previous sections, the chosen topic has been introduced, and key challenges have been identified. The main objectives of the project are formulated as follows:

Design a vector control algorithm for an induction machine drive, oriented in a stator field coordinate system, with no velocity sensors and the ability to run at higher frequencies.

To achieve this objective, the entire process is divided into several subparts:

- *System Representation:* The entire system will be represented by mathematical formulas, establishing a foundation for further analysis and algorithm design.

Regulator Parameter Identification: An approach is devised to obtain the proper parameters for the regulators used in the SFOC strategy. In real-life drive systems, controllers need retuning due to machine parameter variations (in the design process, constant parameters are used). However, the baseline values are determined.

- *Accurate Flux Estimation:* Emphasis is placed on correct flux estimations, crucial for field-oriented control. Open-loop integration in the observer can lead to inaccurate magnitude and angle values, degrading overall control.
- *Speed Estimation*: Proper speed estimation is vital for sensorless control. This is also linked to the accuracy of the flux model, which can be evaluated alongside velocity estimation.

- *System Integration and Testing*: All components will be integrated and tested experimentally to ensure the proposed solution meets the main objective. Initially, this involves running the induction machine at grid frequency. Subsequently, high-speed cases are emulated to verify the theoretical model.

However, the scope of work must be limited due to the broad range of depicted challenges:

- *Motor Parameter Variations:* Variations in motor parameters are not included in the analysis.
- *Low-Speed Case*: The low-speed case is not considered in evaluating the derived algorithm. The obtained results are solely for comparison purposes.
- *Field Weakening Mode*: Field weakening mode is not considered; the reference stator flux remains constant throughout the entire speed range.

1.6 Report structure

This section provides an outline of the report. Each chapter is briefly introduced.

1. **Introduction**: The opening section of the report.
2. **System Modelling**: This chapter represents the drive system using mathematical formulas. The model's correctness is validated using simple scalar control in a MATLAB/Simulink environment. The validated system is then used to test the control algorithm.
3. **Control Algorithm Design**: This chapter details the entire procedure for deriving the control strategy using the MATLAB/SISO Tool package. Proposed estimators are included. The system is tested in simulation with field-oriented control, with simulations conducted in MATLAB/Simulink. The results are discussed and concluded.
4. **Conclusions and Future Work**: This chapter summarizes the results from the entire report and compares them with the objectives outlined in section 1.5. Final conclusions are drawn, and suggestions for future work are presented.

Appendices:

A. **Init Data:** Simulink block diagram in MATLAB for modeling an induction motor

B. **Simulation Models:** Description of the Simulink Block Diagram for Sensorless Control of an Induction Motor Using the Accurate Adaptive Integration Algorithm

2 System Modelling

To create the desired algorithm, it is essential to mathematically represent the system to be controlled. Thus, the following chapter presents the mathematical model of the drive. Initially, necessary assumptions are stated, followed by the formulas describing the system. Finally, it is constructed and validated using simple V/f control to verify its accuracy.

2.1 Induction motor model

For this project, we employ a simplified and idealized model of the squirrel cage induction motor. Hence, we need to outline several assumptions, as specified in [12]:

- The machine is considered a three-phase symmetrical motor.
- Only the fundamental frequency is considered, ignoring higher harmonics.
- Effects such as saturation, iron losses, eddy currents, and temperature dependence are disregarded.
- Resistances and reactances are assumed constant (as concluded from the previous point).
- The three-phase windings (or bars in the rotor cage) are modeled as coils placed in axes shifted by 120°, as depicted in Fig. 2.1.
- Due to simpler formulas, the stationary reference frame is used to model the motor, while the desired control algorithm developed in Chapter 3 is conducted in the rotating reference frame (field-oriented control principle).

To simplify the notation, the three-phase scheme is substituted with the space vector (comprising voltage, current, and flux linkage). The space vector can be defined as follows [12]:

$$\bar{k} \overset{\text{def}}{=} \frac{2}{3}\left[1k_A(t) + \bar{a}k_B(t) + \bar{a}^2k_C(t)\right] \tag{2.1}$$

where,

$$\bar{a} = e^{j2\pi/3} = -\frac{1}{2} + j\frac{\sqrt{3}}{2} \quad ; \quad \bar{a}^2 = e^{j4\pi/3} = -\frac{1}{2} - j\frac{\sqrt{3}}{2} \tag{2.2}$$

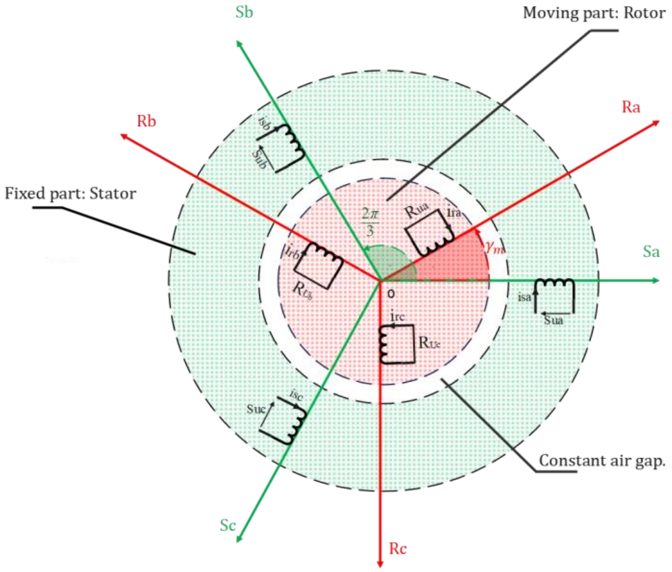

Figure 2. 1: Schematic representation of the three-phase induction motor, illustrating single coils positioned on axes shifted by 120°. The coils represent the stator windings (denoted by uppercase letters - A, B, C) and the rotor bars (denoted by lowercase letters - a, b, c). Additionally, the displacement of the rotor position is indicated by γ_m [12].

and,

$$k_A(t) + k_B(t) + k_C(t) = 0 \tag{2.3}$$

The arbitrary phase quantities in the natural coordinates (A, B, C) are denoted as $k_A(t), k_B(t), k_C(t)$.

However, this representation has a significant drawback: the magnetizing inductance (reactance) depends on the angle γ_m [12], as depicted in Fig. 2.1. This dependency indicates variations with the actual rotor position. To mitigate this issue, it is advisable to transform the vector equations to the common rotating reference frame. For this purpose, the Clarke transformation is employed, which describes the system in the stationary reference frame. The concept is illustrated in Fig. 2.2.

The expression for the Clarke transformation can be formulated as follows [12]:

$$\begin{bmatrix} k_d^s \\ k_q^s \end{bmatrix} = \frac{2}{3} \begin{bmatrix} 1 & -\frac{1}{2} & -\frac{1}{2} \\ 0 & \frac{\sqrt{3}}{2} & -\frac{\sqrt{3}}{2} \end{bmatrix} \begin{bmatrix} k_A \\ k_B \\ k_C \end{bmatrix} \tag{2.4}$$

where ${K_d}^s {K_q}^s$ are the real and imaginary components of an arbitrarily chosen quantity, as previously represented.

where,

${K_d}^s {K_q}^s$are real and imaginary components of arbitrary chosen quantity, represented previously

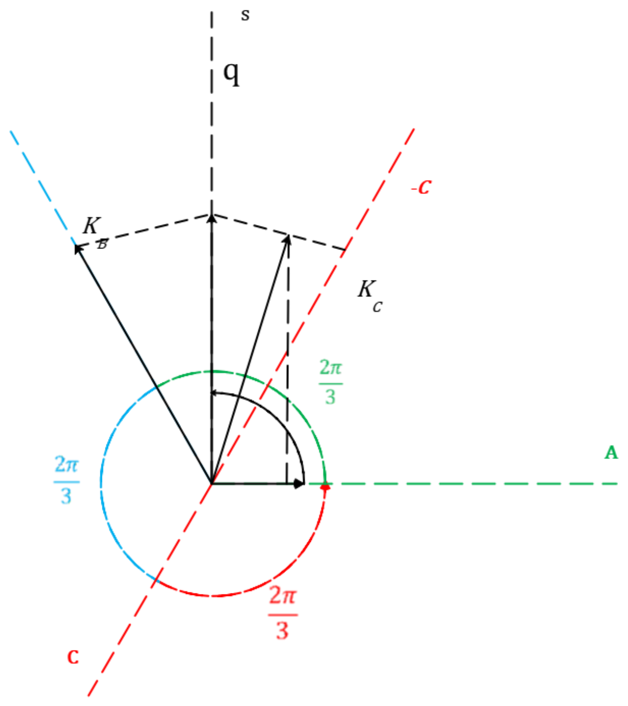

Figure 2. 2: Graphical explanation of the Clarke transformation, transforming values from three phase natural coordinate system to two-axes stationary reference frame. system to two-axes stationary reference frame

in the natural coordinate system, given in the stationary reference frame (denoted by the superscript ‘s’).

Now, it is possible to determine the voltage and flux equations in the new stationary system:

$$u_d^s = R_i^s i_d^s + \frac{d\psi_d^s}{dt} \tag{2.5}$$

$$u_q^s = R_i^s i_q^s + \frac{d\psi_q^s}{dt} \tag{2.6}$$

$$v_d^s = 0 = R_r^s i_d^s + \frac{d\psi_d^s}{dt} + \omega_r \psi_q^s \tag{2.7}$$

$$v_q^s = 0 = R_r^s i_q^s + \frac{d\psi_q^s}{dt} - \omega_r \psi_d^s \tag{2.8}$$

$$\psi_d^s = L_s i_d^s + L_m i_{rd}^s \tag{2.9}$$

$$\psi_q^s = L_s i_q^s + L_m i_{rq}^s \tag{2.10}$$

$$\psi_d^s = L_r i_{rd}^s + L_m i_d^s \tag{2.11}$$

$$\psi_{rq}^{s} = L_r i_{rq}^{s} + L_m i_{q}^{s} \qquad (2.12)$$

where,

$u_{sd}{}^{s}$, $u_{sq}{}^{s}$ are the real and imaginary stator voltage components, respectively, in stationary reference frame,

$u_{rd}{}^{s}$, $u_{rq}{}^{s}$ are the real and imaginary rotor voltage components, respectively, in stationary reference frame,

$i_{sd}{}^{s}$, $i_{sq}{}^{s}$ are the real and imaginary stator current components, respectively, in stationary reference frame,

$i_{rd}{}^{s}$, $i_{rq}{}^{s}$are the real and imaginary rotor current components, respectively, in stationary reference frame,

$\psi_{sd}{}^{s}$, $\psi_{sq}{}^{s}$ are the real and imaginary stator flux components, respectively, in stationary reference frame,

$\psi_{rd}{}^{s}$, $\psi_{rq}{}^{s}$ are the real and imaginary rotor flux components, respectively, in stationary reference frame,

Rs, Rr are the stator and rotor resistances, respectively,

$L_s, L_r, L_m$are the stator, rotor and magnetizing inductances, respectively,

$w_r$is the rotor angular speed (in electrical radians).

In order to complete the model of the motor, expression for the mechanical motion is used:

$$T_e = T_l + J\frac{d\omega_r}{dt} + B\omega_r \qquad (2.13)$$

where,

T_e is the electromagnetic torque,

T_l is the load torque,

J is the inertia,

B is the friction constant.

To connect the input electrical power (defined by the electrical quantities) with the mechanical power, the electromagnetic torque can be expressed as:

$$T_e = \frac{3}{2} p_p L_m \left(i_{sq}^s i_{rd}^s - i_{sd}^s i_{rq}^s \right) \tag{2.14}$$

where

p_p is the number of pole pairs.

Having established all the necessary formulas for the mathematical representation of the motor, the model is constructed in a MATLAB/Simulink environment. The block diagram illustrating the model is presented in Fig. 2.3.

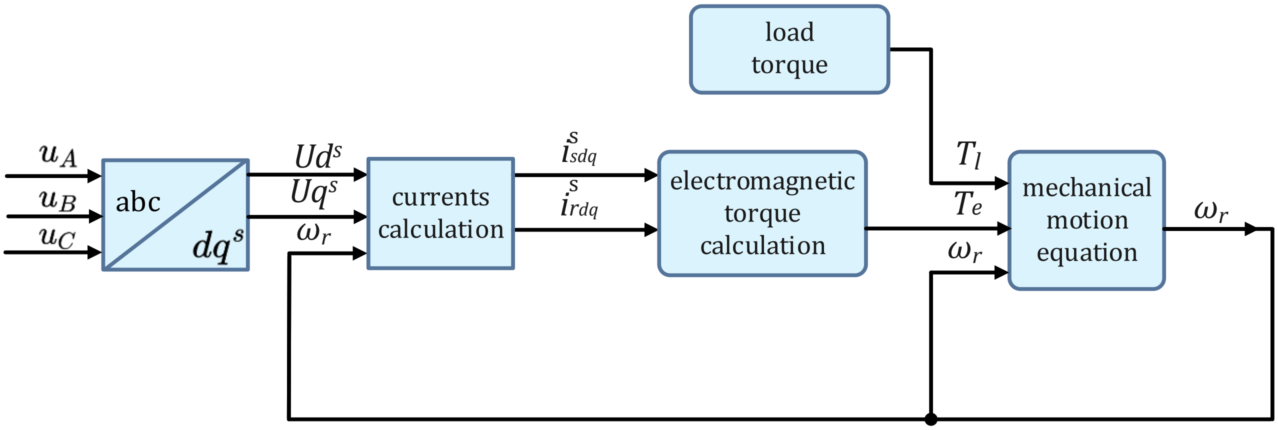

Figure 2. 3: Block diagram presenting complete squirrel cage induction motor model, defined in stationary reference frame.

2.2 Inverter model

To supply the motor, an inverter is utilized. For the sake of the modeling process, its idealized model is employed, defined by the sequence of switching states. The topology of the typical three-phase inverter is shown in Fig. 2.4.

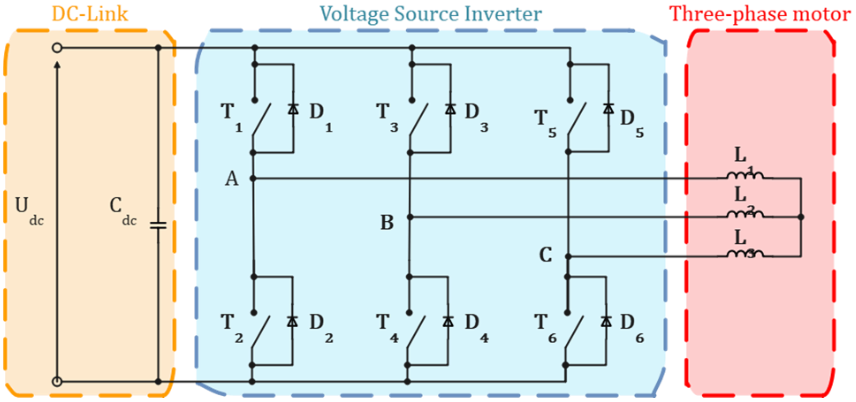

Figure 2. 4: Typical topology of the three-phase inverter.

The load is supplied with line-to-line voltages produced by the converter. It yields:

Load is supplied with line-to-line voltages, produced by the converter. It yields:

$$u_{AB} = u_A - u_B \tag{2.15}$$

$$u_{BC} = u_B - u_C \tag{2.16}$$

$$u_{CA} = u_C - u_A \tag{2.17}$$

where, u_A, u_B, u_C are phase voltages.

$$u_A + u_B + u_C = 0 \tag{2.18}$$

Combining equations (2.15)–(2.17) and (2.18), the proper phase voltages can be formulated as follows:

$$\begin{bmatrix} u_A \\ u_B \\ u_C \end{bmatrix} = \frac{1}{3}\begin{bmatrix} 1 & 0 & -1 \\ -1 & 1 & 0 \\ 0 & -1 & 1 \end{bmatrix}\begin{bmatrix} u_{AB} \\ u_{BC} \\ u_{CA} \end{bmatrix} \tag{2.19}$$

Switching states, mentioned at the beginning of this chapter, are represented by three variables: *DA, DB, DC* Each of them defines the state of one leg of the inverter and can take values '0' or '1' ('0' means the switch is turned off, while '1' indicates it is conducting). Thus, line-to-line voltages can be linked with the DC voltage supplying the converter:

$$\begin{bmatrix} u_{AB} \\ u_{BC} \\ u_{CA} \end{bmatrix} = U_{dc}\begin{bmatrix} 1 & -1 & 0 \\ 0 & 1 & -1 \\ -1 & 0 & 1 \end{bmatrix}\begin{bmatrix} D_A \\ D_B \\ D_C \end{bmatrix} \tag{2.20}$$

The minus sign in (2.20) determines the direction of the current flow (turning on the lower or upper switch, in other words). Inserting equation (2.20) into equation (2.19), the relationship between switching states and phase voltages feeding the motor is obtained:

$$\begin{bmatrix} u_A \\ u_B \\ u_C \end{bmatrix} = \frac{U_{dc}}{3} \begin{bmatrix} 2 & -1 & -1 \\ -1 & 2 & -1 \\ -1 & -1 & 2 \end{bmatrix} \begin{bmatrix} D_A \\ D_B \\ D_C \end{bmatrix} \tag{2.21}$$

The modeled electrical drive is controlled with a space vector modulation (SVM) strategy [13]. The results of simulations are shown in the following section.

2.3 Drive model validation

To verify the correctness of the modeled system, it is decided to run it using a simple V/f algorithm. For simplicity, carrier-based modulation is omitted, and generated duty cycles are directly supplied to the converter. Tests are conducted for $f_{fund} = 50\text{Hz}$ (the nominal frequency of the motor under examination). Necessary parameters for running the simulation are listed in Appendix A.

In the following graphs, the results from the tests are shown. First, the velocity response is presented (Fig. 2.5). It can be observed that initially, the machine rotates at synchronous speed, indicating no-load conditions. Immediately after the load torque is applied to the shaft, the actual rotor velocity is reduced to $n_r = 1431\text{rpm}$.

In the next graph, the phase voltages fed to the motor are depicted (Fig. 2.6). The magnitude of the signals is observed: $\hat{u} = 311.1\text{V}$. This information allows comparison with the rated voltage given by the manufacturer ($u_N = 220\text{V}$). Below, the RMS value is calculated (that expression for RMS computation is valid, as it is assumed, that motor is supplied with ideal, sinusoidal voltage):

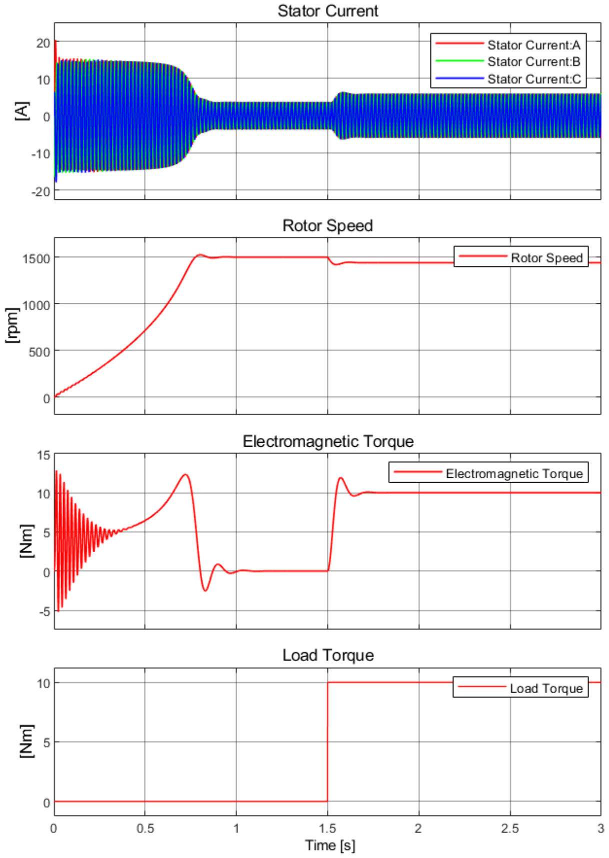

Figure 2. 5: Induction Motor Modeling Results - Stator Current, Rotor Speed, Electromagnetic Torque, and Load Torque

The Figure 2.5 presents the results of the induction motor modeling, showcasing key performance indicators over a simulation period of 3 seconds. The results are illustrated through four main plots: Stator Current, Rotor Speed, Electromagnetic Torque, and Load Torque.

- *Stator Current:*

The plot shows the stator currents for phases A, B, and C. Initially, the currents exhibit high oscillations which gradually stabilize as the motor reaches steady-state operation. This indicates the initial inrush current followed by stable sinusoidal waveforms, demonstrating the motor's ability to handle transient conditions and maintain steady operation.

- *Rotor Speed:*

The rotor speed plot illustrates the motor's speed response. The motor accelerates rapidly to approximately 1500 rpm and then stabilizes, maintaining this speed throughout the simulation period. This confirms the effectiveness of the control algorithm in achieving and maintaining the desired speed.

- *Electromagnetic Torque:*

The electromagnetic torque plot shows the torque response of the motor. Initially, the torque experiences high oscillations, which dampen over time, leading to a steady-state value. This behavior is typical during the motor start-up phase, where the torque stabilizes as the motor reaches its operating speed.

- *Load Torque:*

The load torque plot indicates a step change in load torque, increasing from 0 Nm to 10 Nm at 1.5 second and remaining constant thereafter. This step change is used to test the motor's response to load variations. The motor successfully responds to this change, as reflected in the other plots.

2.4 Summary

In this chapter, two main components of the application (the motor and the inverter) are analyzed and represented by mathematical formulas. These components will be utilized later in testing the exact algorithm. Therefore, it is first necessary to validate if the system is defined correctly. This is accomplished by running the drive with simple scalar control. The inverter is then run with space vector modulation. The results obtained from the tests confirm the sufficient accuracy of the modeled components. Hence, the desired control strategy can be examined.

3 Control Algorithm Design

In the following chapter design process of the chosen strategy is described. It starts from short presentation of principles of field-oriented control. Later on focus is made on deeper analysis of direct stator field oriented control. Afterwards, exact design procedure begins. Additionally, to fulfil the sensorless demand concluded in Chapter 1, flux observer and speed estimator are introduced. Chapter ends with simulation results, verified using the developed system presented in Chapter 2.

3.1 Field oriented control principles

The concept behind using field-oriented control is to achieve ease of machine control, similar to that of DC motors. The torque produced by a DC motor is regulated by varying the armature current, while the excitation current remains constant, maintaining a constant flux. To emulate this behavior in an AC machine, it is necessary to employ a mathematical representation of the motor. Similar to the model presented in Chapter 2, instead of using a stationary reference frame, a rotating coordinate system is utilized.

Obviously, this rotating reference frame can rotate at any speed, but for field-oriented control (FOC), the synchronous speed is chosen. However, it must also be aligned with one of the spinning flux space vectors. Since the flux space vector rotates at synchronous speed, the reference frame speed is selected to be synchronous as well. Hence, there are three types of FOCs: Stator Field Oriented Control (SFOC), Rotor Field Oriented Control (RFOC), and Magnetizing Field Oriented Control (MFOC). The names of these strategies indicate which space vector is chosen for orientation.

Orientation enables the decoupling of currents into two components: the flux component (aligned with the d-axis, the same as the reference space vector) and the torque component (aligned with the q-axis). These components are commanded by reference torque and flux, respectively. Reference torque can be determined by feedback of the actual rotational speed of the motor through a PI regulator. By maintaining the reference flux at a nominal value, the formula for the produced torque (to be presented in the subsequent section) results in a proportional relationship to the reference q-axis current. This clearly shows the similarity to controlling a DC motor.

3.2 Principle of stator field-oriented control

As previously mentioned, to gain the advantages of any field-oriented control, it is necessary to decouple the stator currents (represented by the space vector, rotating in the complex plane) into flux and torque components. In the case of stator field-oriented control, this is done in a synchronously rotating reference frame, aligned with the space vector of the stator flux. Therefore, precise knowledge of its actual position and magnitude becomes crucial. Since the stator flux cannot be directly measured, it must be estimated based on mathematical formulas describing the machine.

However, the very simple expression presented in section 1.3–1.2 suffers from DC offset and drift, causing difficulties in practical implementation. Thus, it is necessary to employ an observer to overcome these drawbacks and obtain reliable information about the flux. A deeper analysis of the problems and proposed solutions is described further in the chapter (section 3.4).

For now, it is assumed that the position and magnitude are perfectly known, allowing the implementation of Stator Field Oriented Control (SFOC). The representation of the discussed current space vector in the chosen reference frame is shown in Fig. 3.1.

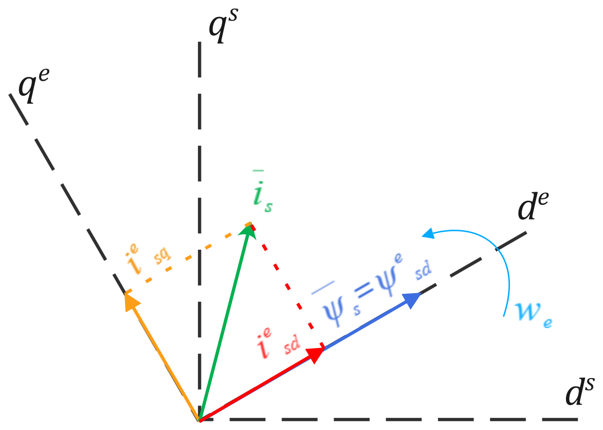

Figure 3. 1: Representation of current space vector in synchronously rotating reference frame, with d-axis alignment with stator flux space vector. Stator flux space vector contains only real component.

The formulas used to build the induction motor model, represented in complex form, are as follows:

$$\overline{u}_s = R_s \overline{i}_s + \frac{d\overline{\psi}_s}{dt} + j\omega_e \overline{\psi}_s \tag{3.1}$$

$$0 = R_r \overline{i}_r + \frac{d\overline{\psi}_r}{dt} + j(\omega_e - \omega_r)\overline{\psi}_r \tag{3.2}$$

$$\overline{\psi}_s = L_s \overline{i}_s + L_m \overline{i}_r \tag{3.3}$$

$$\overline{\psi}_r = L_r \overline{i}_r + L_m \overline{i}_s \tag{3.4}$$

Besides the ability to utilize field-oriented control, orienting the rotating reference frame with the chosen flux space vector significantly reduces the complexity of the expressions. This simplification is due to the elimination of the imaginary component of the flux $\psi_{sq}^e = 0$,consequently $\bar{\psi}_s^e = \psi_{sd}^e + j\psi_{sq}^e = \psi_{sd}^e$(as observed in Fig. 3.1). Hence, the motor equations given in the stator flux synchronous frame are:

$$u_{sd}^e = R_s i_{sd}^e + \frac{d\psi_{sd}^e}{dt} \tag{3.5}$$

$$u_{sq}^e = R_s i_{sq}^e + \omega_e \psi_{sd}^e \tag{3.6}$$

$$u_{rd}^e = 0 = R_r i_{rd}^e + \frac{d\psi_{rd}^e}{dt} - (\omega_e - \omega_r)\psi_{rq}^e \tag{3.7}$$

$$u_{rq}^e = 0 = R_r i_{rq}^e + \frac{d\psi_{rq}^e}{dt} + (\omega_e - \omega_r)\psi_{rd}^e \tag{3.8}$$

$$\psi_{sd}^e = L_s i_{sd}^e + L_m i_{rd}^e \tag{3.9}$$

$$\psi_{sq}^e = 0 = L_s i_{sq}^e + L_m i_{rq}^e \tag{3.10}$$

$$\psi_{rd}^e = L_r i_{rd}^e + L_m i_{sd}^e \tag{3.11}$$

$$\psi_{rq}^e = L_r i_{rq}^e + L_m i_{sq}^e \tag{3.12}$$

where,

ω_e represents the angular synchronous speed. The superscript 'e' denotes a synchronously rotating reference frame.

The calculation of the produced torque is simplified as shown below:

$$T_e = \frac{3}{2} p_p i_{sq}^e \psi_{sd}^e \tag{3.13}$$

The characteristics of the drive being discussed necessitate the consideration of sensorless motor operation. The rationale behind this is detailed in Section 1.4. Consequently, the algorithm's structure is augmented with the estimation of rotational speed, as discussed in Section 3.5. Ultimately, the algorithm can be developed. Its comprehensive structure is illustrated in Figure 3.2.

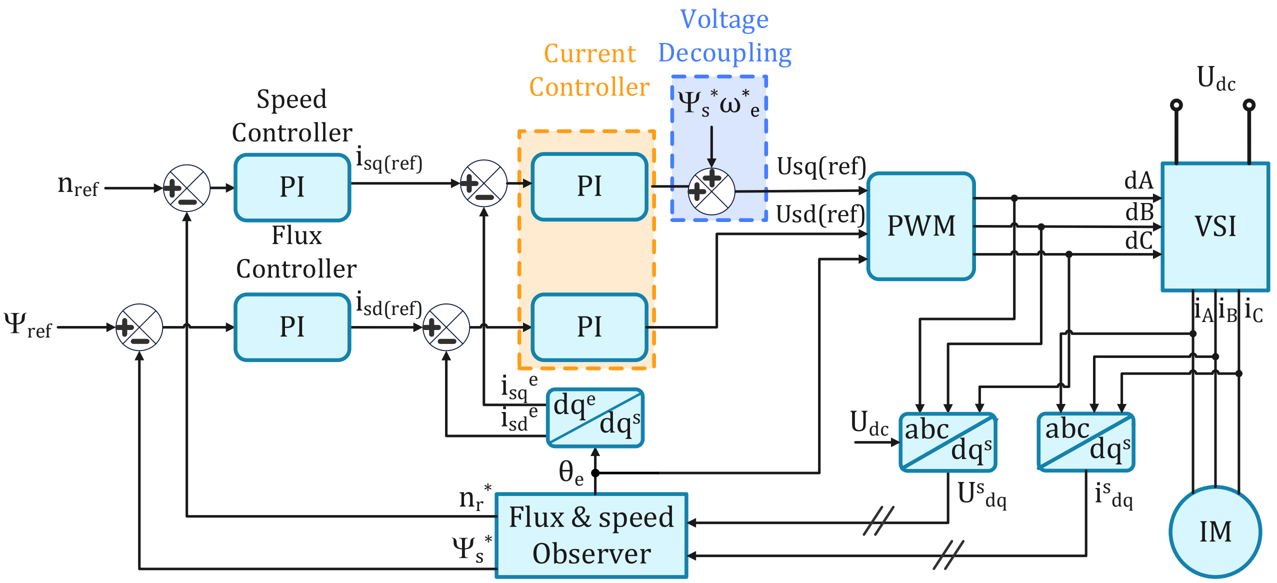

Figure 3. 2: Block diagram presenting stator field-oriented control, run sensorless. The only measurements are phase currents. Voltages required for flux and speed estimations, are calculated with Udc and duty cycles feedbacks. Feedback of the stator flux and rotational speed is obtained with respective estimators - placed together in one block 'Flux & Speed Observer'. [14]

The system depicted in Fig. 3.2 consists of four PI controllers: two for speed and flux regulation, and two for (dq^e) currents regulation. Feedback signals for speed and flux regulators are derived from their respective estimators, which are combined into a single block referred to as the 'Flux & Speed Observer'. Inputs to these observers are voltages and currents represented in the stationary reference frame. Current signals originate from sensors mounted on the wires supplying the machine. Voltage signals are estimated using the DC-link voltage and duty cycles fed to the converter. Additionally, the flux observer provides information about the actual position of the stator flux, which is used to transform the currents from the stationary to the rotating reference frame. These transformed signals are then used as feedback for the current regulators. The current controllers generate reference voltages, and together with the stator flux angle estimation, they are used for space vector modulation techniques. Furthermore, the coupling component existing in the q-axis voltage (3.6) is integrated into the control structure.

The principle in implementing field-oriented control involves representing the stator current space vector in a rotating reference frame. This is achieved with stator flux position information, provided by the flux observer (Fig. 3.2). The transformation is carried out using the Park transformation [12]:

$$\begin{bmatrix} i_{sd}^{e} \\ i_{sq}^{e} \end{bmatrix} = \begin{bmatrix} cos\theta_e & sin\theta_e \\ -sin\theta_e & cos\theta_e \end{bmatrix} \begin{bmatrix} i_{sd}^{s} \\ i_{sd}^{s} \end{bmatrix} \tag{3.14}$$

where,

i_{sd}^{e}, i_{sq}^{e} represent the real and imaginary components of the stator current space vector, respectively, expressed in a synchronously rotating reference frame,

θ_e denotes the stator flux angle, which determines its actual position in the plane.

The concept of the Park transformation is illustrated in Fig. 3.3.

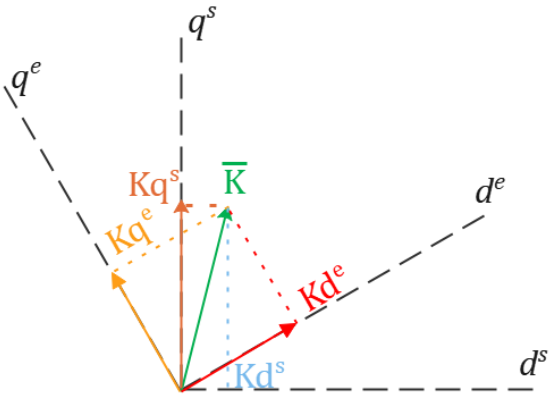

Figure 3. 3: Graphical realization of the Park transformation. k denotes arbitrary chosen space vector. dq^s and $dq^e$are stationary and rotating reference frames, respectively. θ_e determines actual placement of dq^e.

3.3 PI controllers

The control diagram illustrated in Fig. 3.2 incorporates four PI controllers: two for speed and flux regulation, and two for dq^e currents regulation. Their primary objective is to ensure proper and stable operation of the drive. To achieve this, their parameters must be appropriately selected for the controlled drive system. Additionally, they must meet specific requirements:

- Inner (current) regulators: The overshoot should not exceed 4% $(M_p < 4\%)$.
- Outer regulators: These should operate more slowly than the current controllers to maintain system stability.

The transformation to synchronous orientation ensures that the converted currents become direct current (DC) components in steady state. This leads to achieving zero error of the fundamental component [15],[16]. Therefore, current regulators are defined in the synchronous reference frame.

The ordinary PI regulator is represented by the following formula:

$$PI(p) = K_p + \frac{K_i}{p} = K_p \frac{1 + \tau p}{\tau p} \tag{3.15}$$

where,

K_p *and* K_i are the proportional and integral gains, respectively,

τ is the integral time constant,

p is the Laplace operator.

The entire tuning process is divided into four parts:

- d-axis current loop
- d-axis flux loop
- q-axis current loop
- q-axis speed loop

Regulators are adjusted using the MATLAB/SISO tool package. After the tuning process, an anti-windup solution is presented to overcome nonlinearity effects in the control system. The reason for their presence is also explained.

3.3.1 d-axis current loop

Before initiating the exact tuning procedure, it is essential to identify the object to be controlled by the regulator (referred to as the 'plant'). In the case of controlling i_{sd}^e, equation (3.5) is selected, along with (3.9):

$$u_{sd}^e = R_s i_{sd}^e + \frac{d}{dt}(L_s i_{sd}^e + L_m i_{rd}^e) \tag{3.16}$$

From (3.11), it can be derived that:

$$i_{rd}^e = \frac{\psi_{rd}^e - L_m i_{sd}^e}{L_r} \tag{3.17}$$

Substituting this into (3.16) and applying some mathematical manipulation, the result is:

$$u_{sd}^{e} = i_{sd}^{e}(R_s + pL_s') + p\frac{L_m}{L_r}\psi_{rd}^{e} \tag{3.18}$$

where,

$L_s' = L_s - \left(\frac{L_m^2}{L_r}\right)$ is the transient inductance,

p is the Laplace operator, replacing d/dt.

The component $p\frac{L_m}{L_r}\psi_{rd}^{e}$ in (3.18) is regarded as a disturbance and is omitted in further analysis Nevertheless, its presence in the real system is unavoidable unless compensated for. Therefore, the behavior of the regulator, defined based on the simplified transfer function, is validated through tests of the entire control algorithm. Eventually, the transfer function of the plant can be formulated as:

$$G_{i_{sd}(plant)}(p) = \frac{i_{sd}^{e}}{u_{sd}^{e}} = \frac{1}{R_s + pL_s'} = \frac{1}{R_s(pT_s' + 1)} \tag{3.19}$$

where,

$T'_s = \frac{L'_s}{R_s}$

To better represent the real system, certain delays are introduced [17] [18], with respective times:

- **Control algorithm:** Delay corresponding to the time needed for necessary calculations (time constant: T_s);
- **Zero-order-hold (ZOH)**: Delay given by the holding element, maintaining the same value during the sample period (time constant: 0.5 T_s);
- **Inverter:** Delay emulating the presence of the inverter driven by pulse-width modulation (time constant: $0.5T_{PWM}$);
- **Sensor:** Delay introduced by the current sensor, which samples and holds the read value (time constant: 0.5 T_s).

where,

$T_s = \frac{1}{f_s}, T_{PWM} = \frac{1}{f_{PWM}}\ and\ f_s, f_{PWM}$ are the sampling and switching frequencies, respectively (typically chosen to be equal to 5kHz).

The component $p\frac{L_m}{L_r}\psi_{rd}^e$ in (3.18) is considered a disturbance and is neglected in further analysis. However, its presence in the real system is unavoidable unless it is compensated. Therefore, the regulator's behavior is defined based on the simplified transfer function.

$$G_{i_{sd}(plant)}(p) = \frac{i_{sd}^e}{u_{sd}^e} = \frac{1}{R_s + pL_s'} = \frac{1}{R_s(pT_s' + 1)} \tag{3.19}$$

where,

$$T_s' = \frac{L_s'}{R_s}$$

In order to represent better the real system, certain delays are introduced, [17], with respective times:

- **control algorithm** - delay corresponding to time needed for necessary calculations (time constant: Ts);
- **zero-order-hold (ZOH)** - delay given by holding element keeping the same value during sample period (time constant: $0.5Ts$);
- **inverter** - delay emulating presence of the inverter driven by pulse-width modulation(time constant: $0.5Tpwm$);
- **sensor** - delay introduced by the current sensor, which samples and holds read value(time constant: $0.5T_s$).

where,

$T_S = \frac{1}{f_S, T_{PWM}} = \frac{1}{f_{PWM}}$, and f_S, f_{PWM} are sampling and switching frequencies, respectively (they are chosen to be equal to $5kHz$.).

Existing delays, also known as 'transportation lags,' cause no change to occur in the plant until the corresponding time delays elapse. In the time domain, an arbitrary delay can be defined as [19]:

$$y(t) = x(t - T_d) \tag{3.20}$$

where,

$x(t)$ is the input of the transportation lag,

$y(t)$ is the output of the transportation lag,

T_d is the time delay of the transportation lag.

Its transfer function is then:

$$G_{lag}(p) = \frac{Y(p)}{X(p)} = \frac{X(p)e^{-T_d p}}{X(p)} = e^{-T_d p} \qquad (3.21)$$

To include the transportation lag in the analysis, it is preferable to express it as a rational function instead of an exponential form. This can be achieved by using the (p_{pol}, q_{pol}) Padé approximant [17], where (p_{pol}, q_{pol}) are the degrees of the numerator and denominator polynomials, respectively. The approach is to define the exponential and rational functions through the McLaurin series, and then find the coefficients of the numerator and denominator of the rational function. The higher the order of the polynomials of the rational function, the better the precision of the approximant. However, for small delays as previously introduced, it is acceptable to use the (0,1) Padé approximant, which yields [17]:

$$e^{-T_d p} \approx \frac{1}{1 + T_d p} \qquad (3.22)$$

The block diagram of the current closed-loop system, with the regulator, presented delays, and the plant to be controlled, is shown in Fig. 3.4..

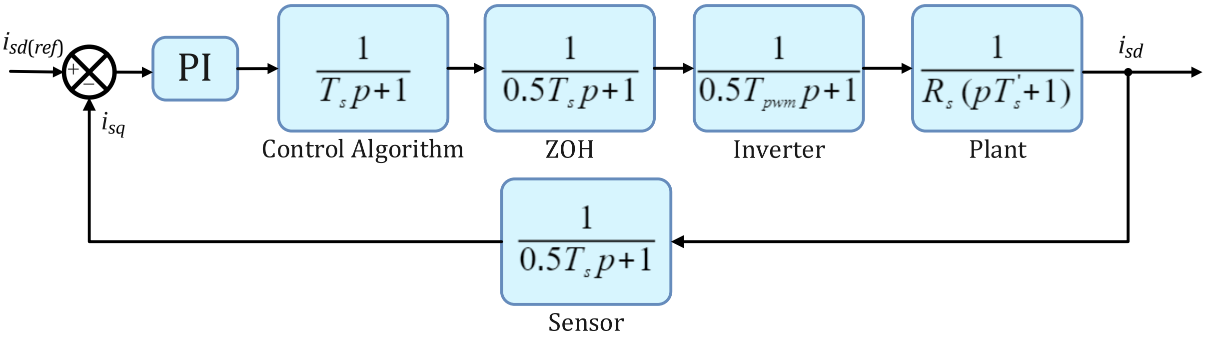

Figure 3. 4: Block diagram of the i_{sd} current close-loop with regulator to be tuned.

As the sensed current signal is sampled, it is necessary to prevent possible aliasing. Typically, this is achieved with an analog anti-aliasing prefilter placed between the sensor and the A/D converter [17]. However, since the current algorithm is designed for a conventional motor (with a nominal stator frequency fstN = 50Hz) and the sampling frequency is chosen to be fs = 5kHz, the sampling theorem of Nyquist and Shannon is satisfied. The theorem states that a sampled signal is appropriately reconstructed if it does not contain frequency components higher than half the sample rate. Therefore, the aforementioned prefilter might be unnecessary.

To simplify further analysis, it is desirable to have unity feedback. Thus, the diagram in Fig. 3.4 can be reformulated, as depicted in Fig. 3.5.

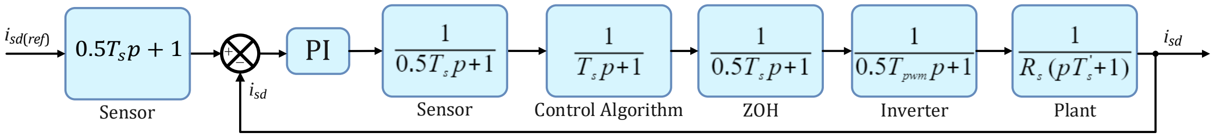

Figure 3. 5 Block diagram of the $(\mathbf{i_{sd}})$ current closed-loop with the regulator to be tuned. Unity feedback is achieved.

Based on Fig. 3.5, the open-loop transfer function of the system can be expressed as:

$$G_{i_{sd}}^{(ol)}(p) = K_{pi_{sd}} \frac{1+p\tau_{i_{sd}}}{p\tau_{i_{sd}}} \frac{1}{0.5T_sp+1} \frac{1}{T_sp+1} \frac{1}{0.5T_sp+1} \frac{1}{0.5T_{pwm}p+1} \frac{1}{R_s(pT_s'+1)} \tag{3.23}$$

Now, the coefficients of the PI regulator can be determined. The first zero of the controllers is chosen to neutralize the effect of the smallest pole, thereby improving the dynamics of the controlled system. The smallest pole is related to the plant, so:

$$\tau_{i_{sd}} = T_s' \tag{3.24}$$

Subsequently, the proportional gain is determined based on the magnitude optimum criterion, where the damping ratio is set to $\zeta = \frac{\sqrt{2}}{2} = 0.707$ [20]. Finally, the parameters are tuned to the following values:

$$K_{pisd} = 20.1264,\ Ki_{isd} = 1720.2,\ \tau_{isd} = 0.0117 \tag{3.25}$$

The response of the d-current control system (considered with the designed controller) to the step command is analyzed. The result is shown in Fig. 3.6.

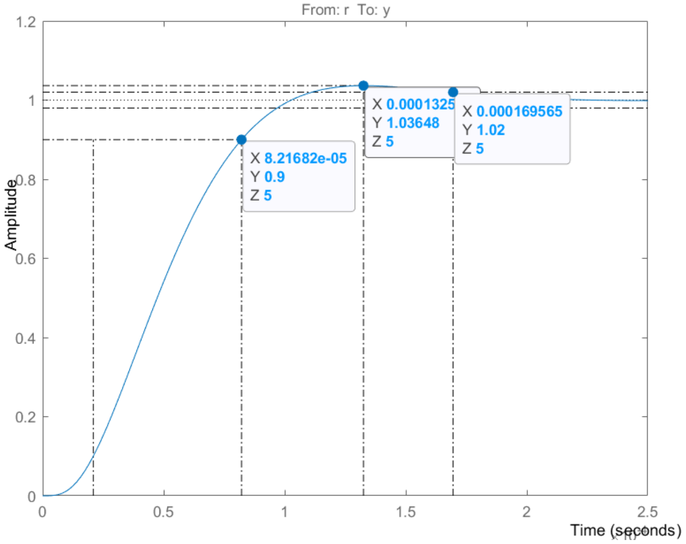

Figure 3. 6: Step response of the system with designed P Iisd controller. Typical characteristics are marked: rising time (tr(10%-90%)) = 0.082168 ms, settling time (ts(2%)) = 0.169565 ms and the maximum overshoot (Mp) = 3.648%. Value '1' on the 'Amplitude' axis denotes arbitrary chosen d-current reference, applied to the control system.

Obtained controller leads to the following properties of the system.

$$\text{tr}(10\%-90\%) = 0.082168 \text{ ms}, \ \text{ts}(2\%) = 0.169565 \text{ ms}, \ \text{Mp} = 3.648\% \qquad (3.26)$$

where,

t_r(10%-90%) is a rising time,

t_s(2%) is a settling time,

$M_p$is a maximum overshoot.

The step response of the system (Fig. 3.6) demonstrates that the regulator operates stably. Additionally, the zero-pole map of the closed-loop system, with the added regulator, is depicted in Fig. 3.7. This also confirms stability, as all poles and zeros are positioned on the left half of the complex plane.

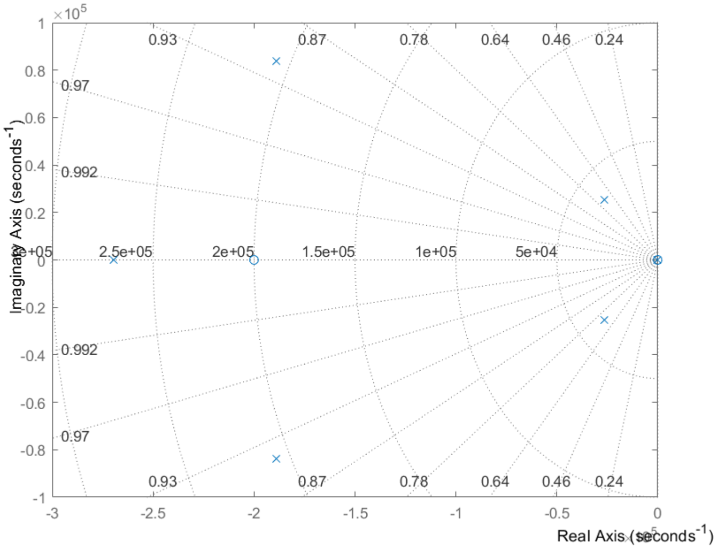

Figure 3. 7: Pole-zero map of the d-current close-loop, including designed regulator. Result indicates stability of the system - all zeros and poles are placed on the left half of the complex plain. Zeros are determined by circles, while poles by crosses

The condition for current controllers, stated in the beginning of the section, is fulfilled.

3.3.2 d-axis flux loop

Regulator used to keep the stator flux at the desired level is tuned by following the similar procedure utilized previously. Therefore, first it is necessary to evaluate transfer function of the plant to be controlled. The evaluation starts from placing (3.11) and (3.12) into (3.7), which yields:

$$0 = R_r i_{rd}{}^{e} + p(L_r i_{rd}{}^{e} + L_m i_{sd}{}^{e}) - (\omega_e - \omega_r) L_r i_{rq}{}^{e} + L_m i_{sq}{}^{e} \tag{3.27}$$

Rotor current components, can be obtained with utilization of (3.9) and (3.10). It results in:

$$0 = R_r \frac{\psi_{sd}^{e} - L_s i_{sd}^{e}}{L_m} + p\left(L_r \frac{\psi_{sd}^{e} - L_s i_{sd}^{e}}{L_m} + L_m i_{sd}^{e}\right) - (\omega_e - \omega_r)\left(-\frac{L_r L_s}{L_m} + L_m\right) i_{sq}^{e} \tag{3.28}$$

After computation process, (3.28) can be reduced:

$$i_{sd}^{e}(pL_\sigma + R_r L_s) = \psi_{sd}^{e}(R_r + pL_r) + L_\sigma s\omega_e i_{sq}^{e} \tag{3.29}$$

where,

$$L_\sigma = L_r L_s - L_m^2$$

$$s\omega_e = (\omega_e - \omega_r) = \frac{(R_r L_s + pL_\sigma) i_{sq}^{e}}{L_r \psi_{sd}^{e} - L_\sigma i_{sd}^{e}}$$

Component: $L_\sigma s \omega_e i_{sq}^e$ in (3.29) is considered as a disturbance, and is ignored in the design process. Similarly, to coupling component in the plant of d-current loop control, given in (3.18), its presence in the real system is not avoidable, unless it is compensated. Thus, the behaviour of the regulator defined on the basis of the simplified transfer function, is verified during tests of entire control algorithm.

After utilization of some mathematical manipulation, transfer function of the plant is formulated:

$$G_{\psi(plant)}(p) = \frac{\psi_{sd}^e}{i_{sd}^e} = \frac{\left(\frac{L_\sigma}{R_r L_s} p + 1\right) R_r L_s}{\left(\frac{L_r}{R_r} p + 1\right) R_r} = L_s \frac{(T_\sigma p + 1)}{(T_r p + 1)} \tag{3.30}$$

where,

$T_\sigma = (L_\sigma / R_r L_S)$

$T_r = \frac{L_r}{R_r}$ is a rotor time constant.

Once, the transfer function of the plant is known, it is necessary to determine the transfer function of the inner loop. Referring to Fig. 3.5, equivalent time constant of the open-loop system can be formulated, as the sum of every small time constants [12]:

$$T_{i_{sd}(ol)}^{eq} = 0.5T_s + T_s + 0.5T_s + T_{pwm} = 0.02ms \tag{3.31}$$

According to used criterion to design the current loop, its close-loop transfer function can be expressed [20]:

$$G_{i_{sd}(cl)}(p) = \frac{1}{2\left(T_{i_{sd}(ol)}^{eq} p\right)^2 + 2T_{i_{sd}(ol)}^{eq} p + 1} \tag{3.32}$$

And the transfer function of entire i_{sd} current control loop, is given:

$$G_{i_{sd}}(p) = (0.5T_s p + 1) \frac{1}{2\left(T_{i_{sd}(ol)}^{eq} p\right)^2 + 2T_{i_{sd}(ol)}^{eq} p + 1} \tag{3.33}$$

Assuming, that:

$$(1 + 0.5T_s p)(1 - 0.5T_s p) = 1 - 0.25T_s^2 p^2 \approx 1 \Rightarrow 0.5T_s p + 1 = \frac{1}{1 - 0.5T_s p} \tag{3.34}$$

transfer function given in (3.33), can be rewritten:

$$G_{i_{sd}}(p) = \frac{1}{1-0.5T_s p}\frac{1}{2\left(T_{i_{sd}(ol)}^{eq}p\right)^2 + 2T_{i_{sd}(ol)}^{eq}p + 1} \quad (3.35)$$

Second order term in (3.35) is much smaller than unity, therefore it is reasonable to neglect it. Hence, equivalent time constant of entire current control loop can be determined:

$$T_{i_{sd}}^{eq} = -0.5T_s + 2T_{i_{sd}(ol)}^{eq} = 0.0375ms \quad (3.36)$$

Approximated transfer function of the inner loop is expressed, eventually:

$$G_{i_{sd}}(p) = \frac{1}{T_{i_{sd}}^{eq}p + 1} \quad (3.37)$$

According to controlled system given in case of current control loop, flux loop consists of only one delay, related to digital calculation. Block diagram presenting the system, is depicted in Fig. 3.8.

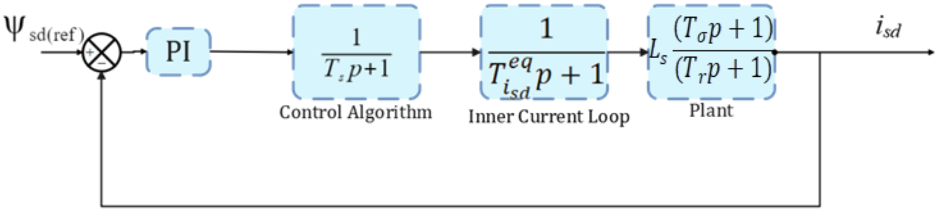

Figure 3. 8: Block diagram of the flux close-loop with regulator to be tuned

Corresponding to Fig. 3.8, open-loop transfer function is given:

$$G_{\psi(ol)}(p) = K_{p\psi}\frac{1+p\tau_\psi}{p\tau_\psi}\frac{1}{T_s p+1}\frac{1}{T_{i_{sd}}^{eq}p+1}L_s\frac{(T_\sigma p+1)}{(T_r p+1)} \quad (3.38)$$

In order to analyze the system, and find coefficient of the controller, transfer function is simplified. Its numerator can be expressed similarly to (3.34):

$$(1+T_\sigma p)(1-T_\sigma p) = 1-0.25T_\sigma^2 p^2 \approx 1 \Rightarrow T_\sigma p + 1 = \frac{1}{1-T_\sigma p} \quad (3.39)$$

Hence, transfer function of the plant becomes of a form:

$$G_{\psi(plant)}(p) = \frac{R_r L_s}{R_r}\frac{1}{T_r p+1}\frac{1}{1-T_\sigma p} = L_s\frac{1}{T_r T_\sigma p^2 + (T_r - T_\sigma)p + 1} \approx L_s\frac{1}{T_\psi p + 1} \quad (3.40)$$

where,

$T_{\Psi} = T_r - T_{\sigma}$

Now, the o pen-loop transfer function (3.38), can be reformulated, and be a basis for further analyses:

$$G_{\psi(ol)}(p) = K_{p\psi} \frac{1 + p\tau_{\psi}}{p\tau_{\psi}} \frac{1}{T_s p + 1} \frac{1}{T_{i_{sd}}^{eq} p + 1} L_s \frac{1}{T_{\psi} p + 1} \tag{3.41}$$

In order to determine coefficients of the PI_{ψ}, *symmetric optimum criterion* ([20], [12]) is applied. Since equivalent time constant of the plant T_{ψ} is small (T_{ψ} = 92.3ms), expression

$$G_{\psi(ol)}(p) = K_{p\psi} \frac{1 + p\tau_{\psi}}{p\tau_{\psi}} \frac{1}{T_s p + 1} \frac{1}{T_{i_{sd}}^{eq} p + 1} L_s \tag{3.42}$$

for the plant can be reduced further [12]

In the open-loop transfer function of the system (3.41), exist two more defined components: $1/(T_s p$ + 1) and $1/(T_{i_{sd}}^{eq} p$ + 1) which time constants are much smaller than one of the plant (T_{ψ}). Thus, these two first-order elements can be reduced, accordingly [12]:

$$G_{\psi(ol)}(p) = K_{p\psi} \frac{1 + p\tau_{\psi}}{p\tau_{\psi}} \frac{1}{T_{\psi}^{eq} p + 1} L_s \tag{3.43}$$

where,

$$T_{\psi}^{eq} = T_s + T_{i_{sd}}^{eq}$$

Consequently, integral time constant of the $PI_{\psi}$is obtained, as:

$$\tau_{\psi} = 4T_{\psi}^{eq} \tag{3.44}$$

Subsequently, proportional gain is tuned, and set of the controller coefficients is found:

$$K_{p\psi} = 19.3398, K_{i\psi} = 10744, \tau_{\psi} = 0.0018 \tag{3.45}$$

In order to study the behaviour of the regulator, response of the flux control loop to the step command is plotted (Fig. 3.9).

Properties of the control loop are obtained:

$$t_{r(10\%-90\%)} = 0.078019\ ms, t_{s(2\%)} = 0.602685ms, M_p = 43.161\% \tag{3.46}$$

Comparing (3.46) to characteristics of corresponding current regulator (PI_{sd}), given in (3.26), rising time is about seven times larger. Its time reaction is in an appropriate level.

In the given step response (Fig. 3.9) is observed very high overshoot, which is the consequence of the chosen criterion [20], [12]. However, that drawback is overcome by current limitation. Similarly to the current controller, it can be concluded, that the system and designed regulator work stable. Response to the step input stabilizes. For additional confirmation, pole-zero map of the flux control loop is plotted in Fig. 3.10.

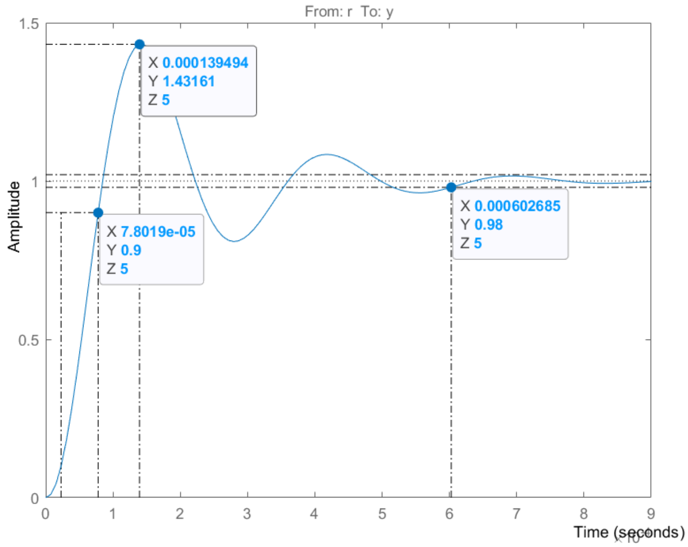

Figure 3. 9: Step response of the system with designed stator flux controller. Typical characteristics are marked: rising time (tr(10%-90%)) =0.078019 ms, settling time (ts(2%)) = 0.602685 ms and the maximum overshoot (Mp) = 43.161%. Value '1' on the 'Amplitude' axis denotes arbitrary chosen stator flux reference, applied to the control system.

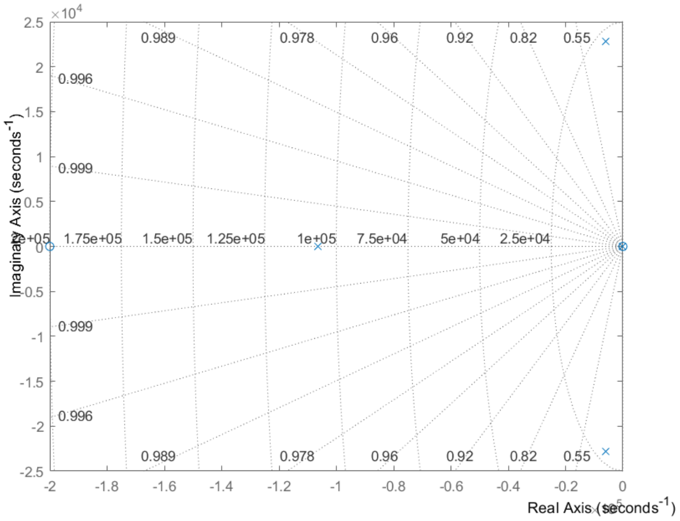

Figure 3. 10: Pole-zero map of the stator flux close-loop, including designed regulator. Result indicates stability of the system - all zeros and poles are placed on the left half of the complex plain. eros are determined by circles, while poles by crosses.

3.3.3 q-axis current loop

Like in previous subsections, transfer function of the object to be controlled has to be determined. Solution starts with (3.6), however, ψ_{sd}^{e} is not omitted:

$$u_{sq}^{e} = R_s i_{sq}^{e} + p\psi_{sq}^{e} + \omega_e \psi_{sd}^{e} \tag{3.47}$$

Then (3.10) is placed into (3.47):

$$u_{sq}^{e} = R_s i_{sq}^{e} + p\left(L_s i_{sq}^{e} + L_m i_{rq}^{e}\right) + \omega_e \psi_{sd}^{e} \tag{3.48}$$

In order to get rid of the rotor current component, (3.8) is used:

$$u_{sq}^{e} = (R_s + pL_s) i_{sq}^{e} - p^2 \frac{L_m}{R_r} \psi_{rq}^{e} - p\frac{L_m}{R_r}(\omega_e - \omega_r)\psi_{rd}^{e} + \omega_e \psi_{sd}^{e} \tag{3.49}$$

Rotor flux q-component appearing in (3.49), can be determined by q-component of stator current: $\psi_{rq}^{e} = i_{sq}^{e}(L_m - L_r L_s / L_m)$Putting that expression into (3.49), yields:

$$u_{sq}^{e} = (R_s + pL_s) i_{sq}^{e} - p^2 \frac{L_m}{R_r}\left(L_m - \frac{L_r L_s}{L_m}\right) i_{sq}^{e} - p\frac{L_m}{R_r}(\omega_e - \omega_r)\psi_{rd}^{e} + \omega_e \psi_{sd}^{e} \tag{3.50}$$

Phrase:$p(L_m/R_r)(\omega_e - \omega_r)\psi_{rd}^{e} + \omega_e \psi_{sd}^{e}$from (3.50) is considered as a disturbance, and is omitted in the analysis. However, the coupling exists in the real system, therefore the behaviour of the regulator defined on the basis of the simplified transfer function, is verified during tests of entire control algorithm.

After several mathematical computational steps, the following result can be obtained:

$$u_{sq}^{e} = i_{sq}^{e} R_s \left(\frac{L_\sigma}{R_r R_s} p^2 + \frac{L_s}{R_s} p + 1\right) \tag{3.51}$$

Finally, transfer function of the plant is found:

$$G_{i_{sq(plant)}}(p) = \frac{i_{sq}^{e}}{u_{sq}^{e}} = \frac{1}{R_s} \frac{1}{\sigma T_{st} T_r p^2 + T_{st} p + 1} \tag{3.52}$$

where,

$T_{st} = \frac{L_s}{R_s}$ is the stator time constant.

System modelled in q-axis current loop, consist of exactly the same delays presented in section 3.3.1. Hence, it might be also represented in the block diagram, as it is shown in Fig. 3.11 (system with sensor delay in the feedback is already replaced by its equivalency with unity feedback).

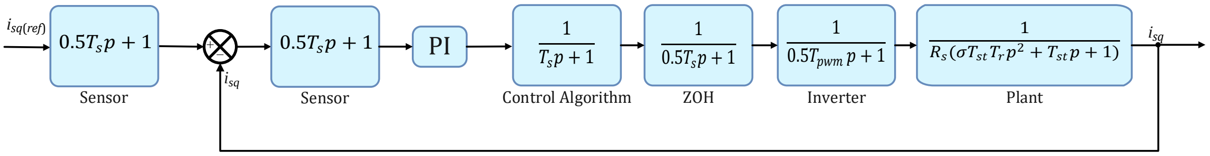

Figure 3. 11: Block diagram of the i_{sq} current close-loop with regulator to be tuned.

Similarly to conclusion obtained in section 3.3.1, anti-alias prefilter is not required, and its presence can be avoided.

From structure of the system given in Fig. 3.11, open-loop transfer function can be formed:

$$G_{i_{sq}(ol)}(p) = K_{pi_{sq}} \frac{1+p\tau_{i_{sq}}}{p\tau_{i_{sq}}} \frac{1}{0.5T_s p+1} \frac{1}{T_s p+1} \frac{1}{0.5T_s p+1} \frac{1}{0.5T_{pwm} p+1} \frac{1}{R_s(\sigma T_{st} T_r p^2+T_{st} p+1)} \tag{3.53}$$

Determining parameters of the PI_{isq}, starts with zero selection. As in previous cases, it is used to cancel the slowest pole of the system (to make the dynamic response improved). In the discussed loop, it is one of poles of the plant ($T_{isq}(1)$ = 56 *ms*, T_{isq} (2) = 56 *ms*). It yields:

$$\tau_{i_{sq}} = T_{i_{sq}(2)} \tag{3.54}$$

Proportional gain is determined with utility of *magnitude optimum criterion*, where the damping ratio is set $\zeta = \frac{\sqrt{2}}{2} = 0.707$ [20]. Eventually, all the parameters are chosen:

$$K_{pi_{sq}} = 8, K_{ii_{sq}} = 142.86, \tau_{i_{sq}} = 5.60e - 02 \tag{3.55}$$

In order to examine the controller behaviour, response of the system to the step command is checked, and the result is presented in Fig. 3.12. It results in the control loop characteristics:

$$t_{r(10\%-90\%)} = 79.1032\, ms, \quad t_{s(2\%)} = 270.62400\, ms, \quad M_p = 3.738\% \tag{3.56}$$

Verification of the stability is made on the basis of pole-zero map of the control loop, presented in Fig. 3.13. Since all the poles and zero are placed on the left half of the complex plain, it is concluded that system is driven stably. Also demand for the controller is fulfilled, as M_p= 3.738% < 4%. However, comparing properties of two current control loops, (3.26) and (3.56), it is easily to note, that PI_{isq}acts slower than PI_{isq} Any trials of improving its reaction lead to instability. The reason of that situation, might be much higher affect of the applied load on q-current component (as it is the torque-producing one). Additionally, its

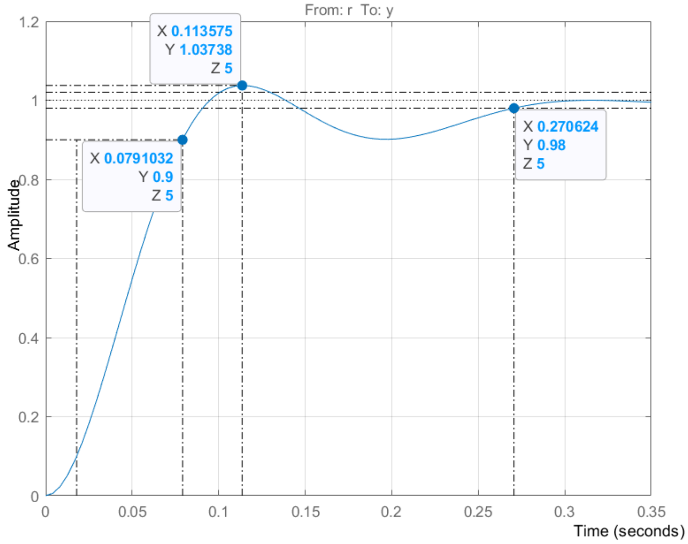

Figure 3. 12: Step response of the system with designed P Iisq controller. Typical characteristics are marked: rising time (tr(10%-90%)) = 79.1032 ms, settling time (ts(2%)) = 270.62400 ms and the maximum overshoot (Mp) = 3.738%. Value ’1’ on the ’Amplitude’ axis denotes arbitrary chosen q-current reference, applied to the control system.

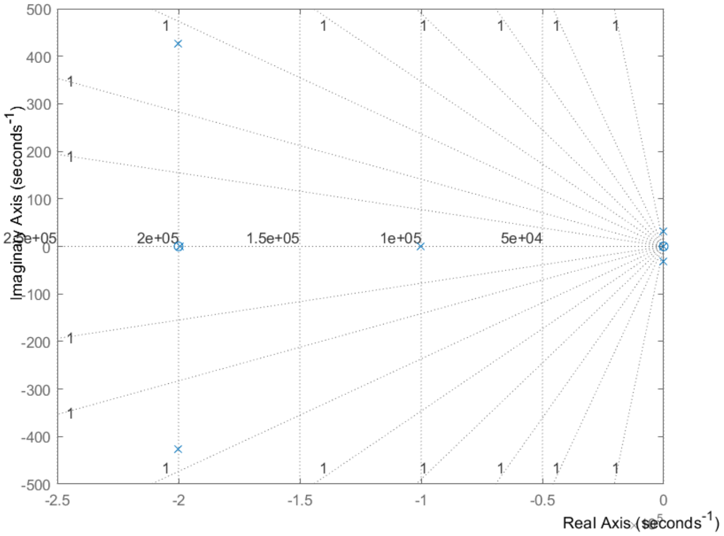

Figure 3. 13: Pole-zero map of the q-current close-loop, including designed regulator. Result indicates stability of the system - all zeros and poles are placed on the left half of the complex plain. Zeros are determined by circles, while poles by crosses.

controller is designed with *magnitude optimum criterion*, which is not the optimal solution for systems with presence of disturbances [20]. Nevertheless, *symmetric optimum criterion*, which overcomes above drawback, is characterized by very big overshoot, what, in case of current controllers criteria set in the beginning of the section, is unacceptable.

3.3.4 q-axis speed loop

The controlled plant for speed regulator is formulated from (3.13):

$$G_{\omega(plant)}(p) = \frac{T_e}{i_{sq}^e} = \frac{3}{2} p_p \psi_{sd}^e \qquad (3.57)$$

To obtain the feedback signal for the speed command, (2.13) is used. Actual design is made for conventional induction motor, which friction constant is negligibly small. Thus, the formula can be reduced:

$$T_e = T_l + Jp\frac{\omega_r^{el}}{p_p} \Rightarrow \omega_r^{el} = (T_e - T_l)\frac{p_p}{Jp} \qquad (3.58)$$

where,

$\omega_r^{el} = \omega_r p_p$is an electrical angular rotor speed

However, the resulting speed depends also on the load torque, which is treated as the disturbance. Therefore, the procedure applied to design speed controller, slightly differ from previously utilized. Nevertheless, first, transfer function of the inner current loop has to be formulated. It begins from calculating equivalent open-loop time constant. As, only the slowest pole of the plant of q-current loop is cancelled by its regulator, the second one is included in equivalent time constant computation:

$$T_{i_{sq}(ol)}^{eq} = T_{i_{sq}(1)} + 0.5T_s + T_s + 0.5T_s + T_{pwm} = 56.3ms \qquad (3.59)$$

Close-loop transfer function of the system given in Fig. 3.11, with calculated equivalent time constant is formulated, as:

$$G_{i_{sq}(cl)}(p) = \frac{1}{2\left(T_{i_{sq}(ol)}^{eq} p\right)^2 + 2T_{i_{sq}(ol)}^{eq} p + 1} \qquad (3.60)$$

Including the system element appeared before the node (Fig. 3.11) into to transfer function of entire q-current loop, yields:

$$G_{i_{sq}}(p) = (0.5T_s p + 1)\frac{1}{2\left(T_{i_{sq}(ol)}^{eq} p\right)^2 + 2T_{i_{sq}(ol)}^{eq} p + 1} \qquad (3.61)$$

Accordingly, to the assumption (3.34), (3.61) can be rewritten:

$$G_{i_{sq}}(p) = \frac{1}{1-0.5T_s p}\frac{1}{2\left(T^{eq}_{i_{sq}(ol)}p\right)^2 + 2T^{eq}_{i_{sq}(ol)}p + 1} \tag{3.62}$$

Second order component in (3.62) is much smaller than unity, and can be neglected. Thus, $G_{i_{sq}}(p)$ is reduced to first-order system. Time constant of entire q-current loop is computed:

$$T^{eq}_{i_{sq}} = -0.5T_s + 2T^{eq}_{i_{sq}(ol)} = 112.6\,ms \tag{3.63}$$

And resulting, approximated transfer function is:

$$G_{i_{sq}}(p) = \frac{1}{T^{eq}_{i_{sq}}p + 1} \tag{3.64}$$

As the system is run sensorless (Fig. 3.2), there is no sensor providing feedback for the control algorithm (no delay in the feedback). The only one-time delay considered in actual process is related to digital calculations. But, as it is mentioned previously, system and the design procedure differ, due to disturbance signal consideration, as it is visible in Fig. 3.14.

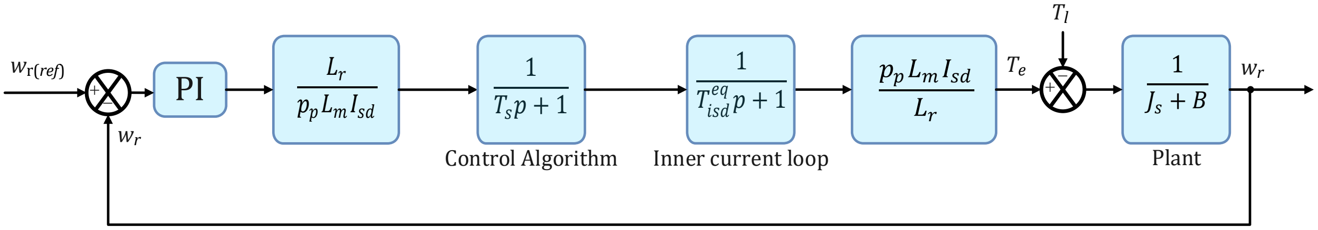

Figure 3. 14: Block diagram of the speed close-loop with regulator to be tuned. Load torque disturbance is added to the system.

Analyzed system is considered linear, thus it is resolved with superposition usage[18]. First ω_r^{el} is treated as an input of the system, and T_l is set to zero. Afterwards, input torque is examined, while the speed is kept zero.

In the first case, only proportional part of the regulator is utilized [18], as it is shown in Fig. 3.15.

Open-loop transfer function of the system given in Fig. 3.15, is formulated:

$$G_{\omega(ol)}(p) = K_{p\omega}\frac{1}{T_s p + 1}\frac{1}{T^{eq}_{i_{sq}}p + 1}\frac{1}{Jp + B} \tag{3.65}$$

By defining equivalent time constant,

$$T^{eq}_{\omega} = T_s + T^{eq}_{i_{sq}} \tag{3.66}$$

transfer function in (3.65), can be simplified to the first-order system:

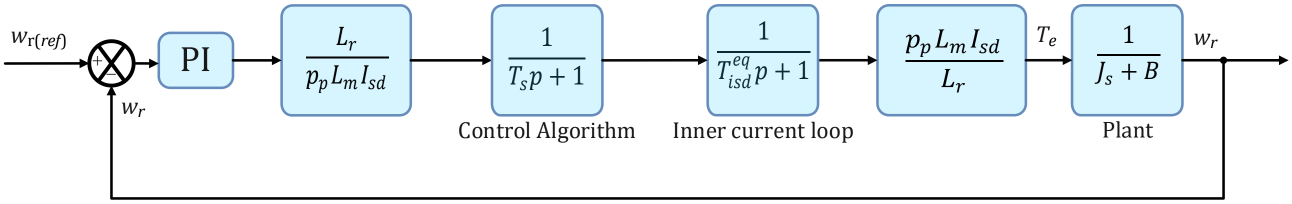

Figure 3. 15: Block diagram of the speed close-loop with regulator to be tuned. Only speed input is taken into account.

$$G_{\omega(ol)}(p) = K_{p\omega}\frac{1}{T_{\omega}^{eq}p+1}\frac{1}{Jp} \tag{3.67}$$

In order to find optimal solution, *magnitude optimum criterion* is used. Tuned coefficient of the controller is given:

$$K_{p\omega} = 1 \tag{3.68}$$

In order to find the parameters of the integral part of the regulator, second case is studied (load torque is considered as an input to the system, while speed is set to zero).

That situation is observed in Fig. 3.16

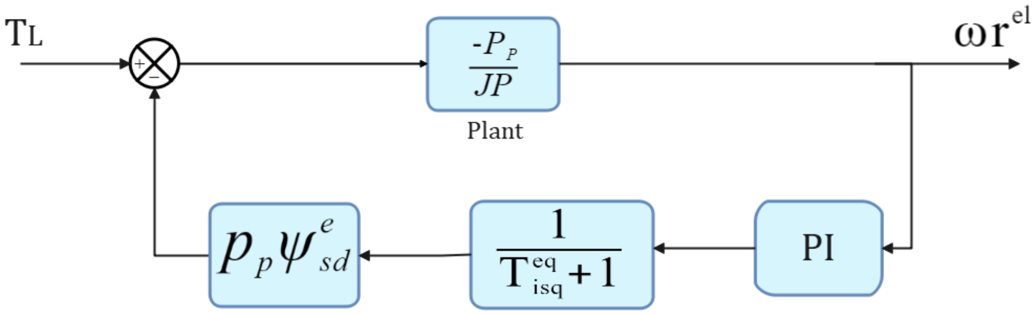

Figure 3. 16: Block diagram of the speed close-loop with regulator to be tuned. Load torque is considered as an input to the system, while speed is set to zero

Control scheme presented in Fig. 3.16, is described by the following transfer function:

$$\frac{\omega_r(p)}{T_l(p)} = \frac{-\frac{p_p}{Jp}}{1+\left(-\frac{p_p}{Jp}\right)\left(-\frac{3}{2}p_p\psi_{sd}^{e}\frac{1}{T_{\omega}^{eq}p+1}K_{\omega}\frac{1+\tau_{\omega}p}{\tau_{\omega}p}\right)} \tag{3.69}$$

After several mathematical manipulations (3.69) is reduced to:

$$\frac{\omega_r(p)}{T_l(p)} = -\frac{p_p}{J}\frac{2\tau_\omega T_\omega^{eq} p\left(T_\omega^{eq} p + 1\right)}{2\left(T_\omega^{eq}\right)^2\tau_\omega p^3 + 2T_\omega^{eq}\tau_\omega p^2 + \tau_\omega p + 1} \tag{3.70}$$

Due to the character of the studied system, *symmetric optimum criterion* is chosen to determine the time constant of the integral controller:

$$\tau_\omega = 4T_\omega^{eq} \tag{3.71}$$

Complete set of sought coefficients of $PI_\omega$is given:

$$K_{p\omega} = 1, K_{i\omega} = 2.8662, \tau_\omega = 0.3489 \tag{3.72}$$

In order to examine the stability in case of disturbance (load torque) presence, pole-zero map of (3.70) is plotted, and presented in Fig. 3.17. It shows that, all poles (determined by the crosses) are placed in the left part of the plain, what indicates stability of the system.

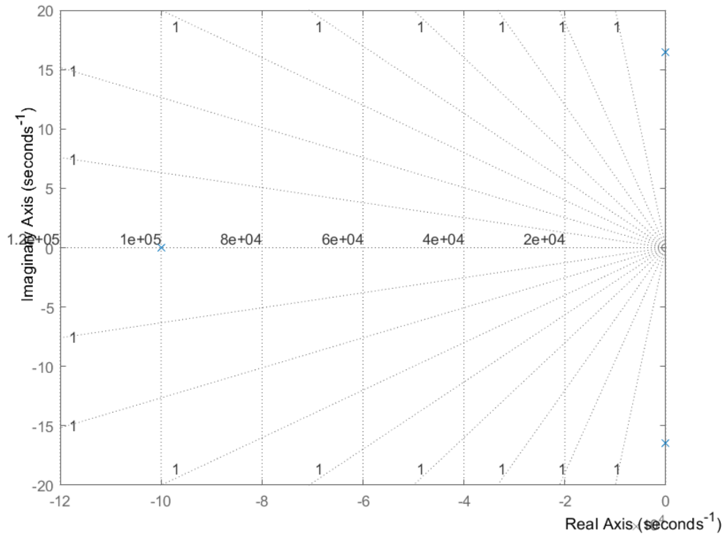

Figure 3. 17: Pole-zero map of the speed close-loop with consideration of the load torque. Result indicates stability of the system. Zeros are determined by circles, while poles by crosses.

Properties of the designed speed regulator are studied with step response of control loop, while disturbance is not considered. The result is shown in Fig. 3.18. Characteristics of the loop, are listed below:

$$t_{r(10\%-90\%)} = 102.28500\ ms, t_{s(2\%)} = 824.02600\ ms, M_p = 42.74\% \tag{3.73}$$

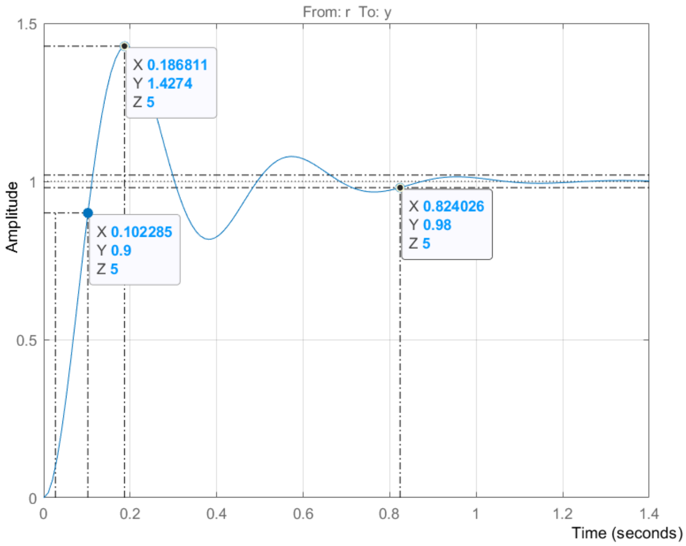

Figure 3. 18: Step response of the system with designed controller, without load torque input consideration. Typical characteristics are marked: rising time (tr(10%-90%)) = 102.28500 ms, settling time (ts(2%)) = 824.02600ms and the maximum overshoot (Mp) =42.74%. Value '1' on the 'Amplitude' axis denotes arbitrary chosen speed reference, applied to the control system.

The requirement for the outer-loop regulators (including the speed regulator) is to be slower than the corresponding current regulator. Comparing the characteristics of the speed control loop (3.73) and the corresponding q-current loop (3.56), it is evident that the current loop operates faster.

3.3.5 Integrator anti-windup

Each of the designed controller outputs must be limited to prevent hardware damage (e.g., from overcurrent or overvoltage). These limitations introduce nonlinearities into the system. When the regulator's output is sufficiently high, the signal sent to the controlled object reaches the saturation level, causing the integral part to continue integrating the supplied error. This results in the controller's output increasing (winding up). This continues until the plant feedback exceeds the reference value, and a negative error appears in the PI input. This change causes the integral part to produce a high output to compensate for the previously accumulated error, leading to overshoots in the responses. If the signal remains saturated for a significant amount of time, it could deteriorate control and render the system unstable.

To overcome this situation, an anti-windup mechanism is added to each controller [17]. Its basic structure is presented in Fig. 3.19.

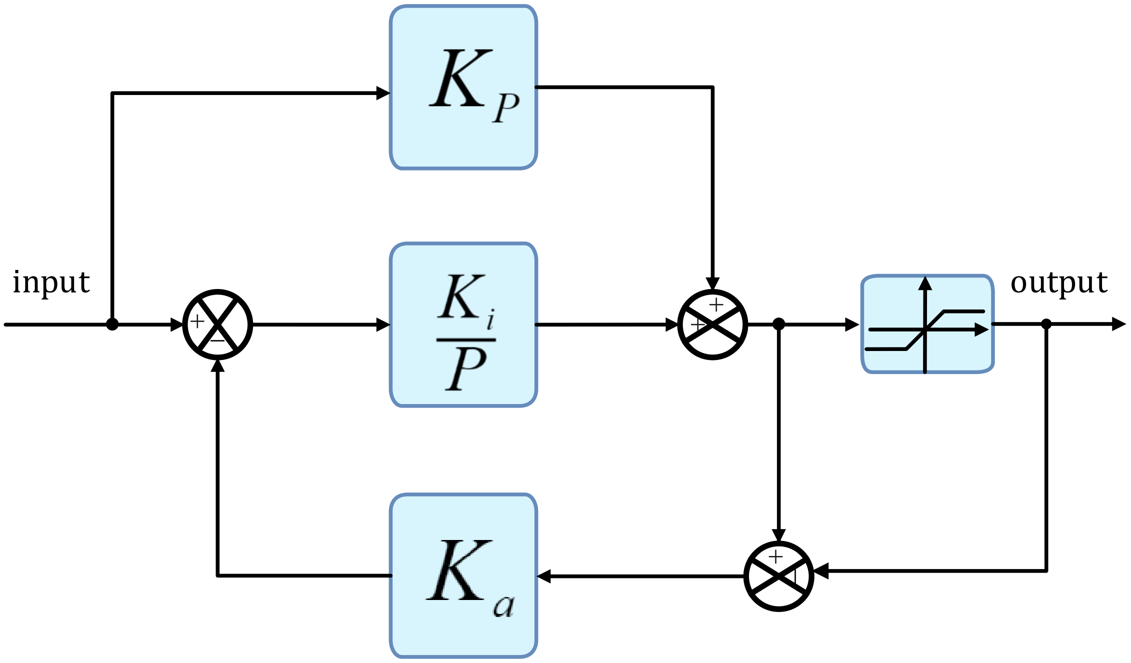

Figure 3. 19: Integrator antiwindup technique, to cancel the effect of the saturations.

Antiwindup gains should be selected to keep the input of the integrator relatively small, whenever the saturation occurs [17]. Hence, respective gains are chosen:

$$K_{ai_{sd}} = 5 \tag{3.74}$$
$$K_{a\psi} = 10 \tag{3.75}$$
$$K_{ai_{sq}} = 100 \tag{3.76}$$
$$K_{a\omega} = 90 \tag{3.77}$$

3.4 Stator flux observer

The introduction to this chapter emphasizes that a crucial part of the stator field-oriented control is the precise knowledge of the stator flux magnitude and its actual position. As the design is focused on enabling the algorithm to run the motor sensorless, this information can be estimated. In the case of stator field orientation, it is realized by a simple expression (3.12). Besides simplicity, problems related to the signal integration are known. In physical implementation, the result of the ideal integration is affected by the offset and drift [21]-[22]. The source of the first problem comes from non-perfect measurements of current and/or voltages, while the second one exists because of the method of integration.

Considering $x(t)$ as the ideal, arbitrary signal to integrate, the corresponding measured one is always introduced with offset (due to imperfections of used sensors). Therefore, after its integration, one can obtain:

$$\int x_{meas}(t)dt = \int \left[x(t) + x_{off}\right]dt = y(t) + tx_{off} + C \tag{3.78}$$

where,

$y(t)$ is the integral of $x(t)$,

x_{off} is the offset value of the measured signal,

C is the constant value resulting from initial conditions of the integral

Additionally, to derive accurate flux information, the exact value of the stator resistance must be known. However, its influence is dominant at low speed range, while in high speed case the problem vanishes [21]. Thus, it is not further investigated.

Several solutions discussed in the literature propose ways to overcome these drawbacks. Among them, three are highlighted:

- Low-pass filter (LPF) based model,
- High-pass filter (HPF) based model,
- Voltage-current model.

All of them present good results over a wide speed range. However, a few specific characteristics are considered. In the case of LPF-based models, to compensate for phase and magnitude distortions, an interior feedback loop is designed together with the PI regulator [23]. This requires additional tuning procedures, complicating the process. A suggestion to avoid this is using programmable LPF, which limits the dependency on the actual speed [21], [24]. However, this solution is not further explored.

The voltage-current model yields good estimation results [23, 25], but requires speed/position feedback, which in sensorless control becomes very precise and critical. Small errors in the velocity estimation will be amplified in the flux calculations.

The HPF-based model is selected for final investigation and eventual implementation. It requires phase and magnitude compensators but does not need a feedback loop or an additional controller [23], [26]. Therefore, for the final investigation and actual implementation, the HPF-based model is chosen.

Among the proposed structures of the estimator, the basic architecture is adopted [26]. Its representation is shown in Fig. 3.20.

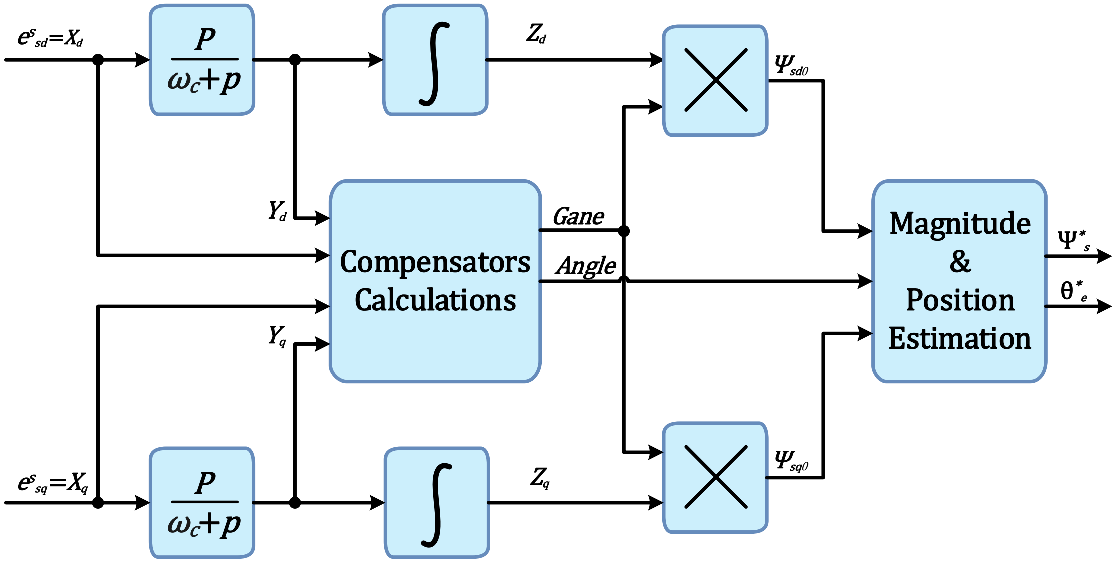

Figure 3. 20: Basic structure of the HPF-based model of the stator flux estimator [26].

The reason of usage high-pass filters is to get rid of the dc-offset in the signal to be integrated. Applied filters are first order filters, hence signal with lower frequencies than cut-off frequency is not completely attenuated. Therefore, after passing filtered out signal through pure integrator, flux can be reconstructed with phase and gain compensators, as it is visible in Fig. 3.20.

In order to evaluate the observer, set of formulas has to be introduced. First, the high pass filter is defined. It can be given by means of transfer function:

$$HPF(p) = \frac{p}{p+\omega_c} \tag{3.79}$$

where,

$$\omega_c = 2\pi f_c$$

and,

f_c is the cut-off frequency.

$$Gain = \sqrt{\frac{X_d^2 + X_q^2}{Y_d^2 + Y_q^2}} \tag{3.80}$$

$$Angle = atan2\left(sin(\theta_y - \theta_x), cos(\theta_y - \theta_x)\right) \tag{3.81}$$

Afterwards, parameters of the compensators, are calculated:

where,

$X_d X_q$are the signals applied to HPFs (back EMFs),

$Y_d Y_q$are the outputs of HPFs,

$\theta_x \theta_y$are the angles of back EMF, before and after HPFs, respectively.

Positions: $\theta_x \theta_y y$, used in (3.81), are given as:

$$\theta_x = atan2(X_q, X_d) \tag{3.82}$$

$$\theta_y = atan2(Y_q, Y_d) \tag{3.83}$$

Calculated compensators (3.80), (3.81) are used to determine the desired stator flux information:

$$\hat{\psi}_s^* = \sqrt{\psi_{sd0}^2 + \psi_{sq0}^2} \tag{3.84}$$

$$\theta_e^* = atan2(sin(\theta_{e0} - Angle), cos(\theta_{e0} - Angle)) \tag{3.85}$$

where,

ψ_{sdo} = $Gain \cdot Z_d$

ψ_{sqo} = $Gain \cdot Z_q$

θ_{eo} = $atan2$ (ψ_{sqo}, ψ_{sdo}) = $atan2(Z_q, Z_d)$

and,

Z_d, Z_q, are the outputs of pure integrator of d and q axis, respectively.

Besides its simplicity, simulation tests give unaccepted results. The reason of that, might be presence of derivations in the inputs of the observer (caused by the HPFs). As it is suggested to avoid any derivative parts, idea presented in [22] is utilized. Looking again into transfer function of high-pass filter, it can be rephrased, in a certain way:

$$HPF(p) = \frac{p}{p + \omega_c} = \frac{p + \omega_c - \omega_c}{p + \omega_c} = 1 - \frac{\omega_c}{p + \omega_c} \tag{3.86}$$

Simple mathematical manipulation introduced in (3.86), shows that HPF can be introduced by its equivalency containing low-pass filter. In that way, undesirable derivatives disappear.

Proper working of the estimator is assured, when cut-off frequency of filters fulfil two conditions [26]. It has to be much higher than inverse of stator time constant of the motor to be driven, and it ought to be lower than sampling frequency. Observing responses for few values of cut-off frequency, finally it is set to ω_c = 1500 *rad/s*, what corresponds to f_c= 238.73*Hz*. Below, comparison with fulfilled requirements is done:

$$\frac{1}{T_{st}} = \frac{R_s}{L_s} = 20Hz \ll f_c = 400Hz < f_s = 5000Hz \tag{3.87}$$

The performance of the derived observer is shown together with drive simulation, which is done in section 3.6.

3.5 Speed estimator

Next to observer described in previous subsection, there is a request for speed estimator, in order to fulfil sensorless control demand. As in case of asynchronous motor exists slip, which introduces difference between rotor speed and synchronous speed, sought estimation of the velocity can be determined:

$$\omega_r^* = \omega_e^* - \omega_{sl}^* \tag{3.88}$$

where,

${\omega_r}^* {\omega_e}^* {\omega_{sl}}^*$are the rotor, synchronous and slip angular speed estimations, respectively.

Synchronous speed estimation can be obtained from steady-state approximation [27]:

$$p\overline{\psi}_s \approx j\omega_{e\overline{\psi}_s} \Rightarrow \omega_e = \frac{1}{j\overline{\psi}_s} p\overline{\psi}_s \tag{3.89}$$

After mathematical manipulation, final formula for synchronous angular speed is achieved:

$$\omega_e^* = \frac{\psi_{sd}^{s*} p\psi_{sq}^{s*} - \psi_{sq}^{s*} p\psi_{sd}^{s*}}{(\hat{\psi}_s^*)^2} = \frac{\psi_{sd}^{s*} e_{sq}^{s*} - \psi_{sq}^{s*} e_{sd}^{s*}}{(\hat{\psi}_s^*)^2} \tag{3.90}$$

where,

${\psi_{sd}}^{s*}, {\psi_{sq}}^{s*}$are the estimated stator flux d and q components, respectively,

${e_{sd}}^{s*}, {e_{sq}}^{s*}$are the estimated back EMF d and q components, respectively.

Similarly to synchronous angular speed, slip has to be introduced by typical, electrical measurements. Therefore, analysis begins from *simplified Kloss formula*, linking slip and the produced torque [12]:

$$T_e = T_k \frac{2}{\left(\frac{\omega_{sl}}{\omega_{slk}}\right)^2 + \left(\frac{\omega_{slk}}{\omega_{sl}}\right)^2} \tag{3.91}$$

where,

T_K is the breakdown torque,

ω_{slk} is the breakdown angular slip velocity.

In case of high speeds, actual slip becomes much smaller than the breakdown one: $\omega_{sl} \ll \omega_{slk}$. Thus, expression (3.91) can be further simplified [12]:

$$\frac{T_e}{T_k} = \frac{2\omega_{sl}}{\omega_{slk}} \tag{3.92}$$

Breakdown torque is given by the relation:

$$T_k \sim \left(\frac{u_s}{\omega_e}\right)^2 \approx \psi_s = const \tag{3.93}$$

It is valid, if $R_s = 0$ In high-speed region, effect of the resistance diminishes, therefore (3.93) provides that breakdown torque remains constant. Additionally, (3.91) is applicable to any torque, also, the nominal one [28]. It yields:

$$\frac{T_e}{T_k} = \frac{\omega_{sl}}{\omega_{sln}} \tag{3.94}$$

where,

T_{eN} is the nominal electromagnetic torque,

ω_{slN} is the nominal slip angular speed.

In order to determine the actual torque of the motor, utilizing only standard measurements, method described in [29] is used. The idea of the solution is to determine stator flux space vector in the rotating reference frame oriented with $\bar{u}_{s\psi}$ space vector ($\bar{u}_{s\psi}$ is aligned with its d-component), which is defined as following:

$$\overline{u}_{s\psi} = j\omega_{e\overline{\psi}_s} \tag{3.95}$$

Chosen orientation, yields:

$$\overline{u}_{s\psi} = u^e_{sd\psi} \Rightarrow u^e_{sd\psi} = -\omega_e \psi^e_{sq} \Rightarrow \psi^e_{sq} = -\frac{u^e_{sd\psi}}{\omega_e} \tag{3.96}$$

Now, torque can be related to obtained flux, according to the relation:

$$T_e = \frac{3}{2} p_p \Im\left(\overline{\psi}_{s_{conj}} \cdot \bar{\iota}_s\right) = \frac{3}{2} p_p \Im\left[j \frac{u^e_{sd\psi}}{\omega_e} \cdot \left(i^e_{sd} + j i^e_{sq}\right)\right] = \frac{3}{2} p_p \frac{u^e_{sd\psi}}{\omega_e} i^e_{sd} = const \cdot i^e_{sd} \tag{3.97}$$

$\Im$ indicates imaginary part of the complex number,

$\overline{\psi}_{s_{conj}}$ is the conjugated stator flux space vector.

Result obtained in (3.97), leads to the final solution for the slip angular estimation:

$$\frac{T_e}{T_{eN}} = \frac{i^e_{sd}}{i^e_{sdN}} \Rightarrow \frac{\omega_{sl}}{\omega_{slN}} = \frac{i^e_{sd}}{i^e_{sdN}} \Rightarrow \omega_{sl} = \frac{i^e_{sd}}{i^e_{sdN}} \omega_{slN} \tag{3.98}$$

Additionally, low-pass filters are placed before each estimation $\left(\omega_r{}^* \omega_e{}^* \omega_{slip}{}^*\right)$.Cut-off frequencies are selected by observations of the plotted results of the signals. It yields:

$$LPF_{\omega_e}(p) = \frac{50}{p + 50} \tag{3.99}$$

$$LPF_{\omega_r}(p) = \frac{100}{p + 100} \tag{3.100}$$

$$LPF_{\omega_{slip}}(p) = \frac{100}{p + 100} \tag{3.101}$$

Presented method relies only on the current measurements, and voltage estimations from inverter states, what definitely fulfils sensorless objective.

3.6 Simulation results

This section presents the performance analysis of sensorless control of an induction motor using the Accurate Adaptive Integration Algorithm. The analysis includes the evaluation of speed, stator angle, torque, and flux responses. The results demonstrate the algorithm's capability to effectively control the motor, with specific areas identified for further refinement to enhance accuracy and stability.

Speed Response Analysis:

The top plot illustrates the speed response of the induction motor. The reference speed, indicated by the dashed line, is closely followed by both the measured speed (blue line) and the estimated speed (red line). Key observations include:

- *Initial Acceleration (0 to 2 seconds):* The reference speed increases linearly to 50 rad/s. The estimated speed follows closely with minimal lag, while the measured speed shows a slight delay.
- *Steady-State (2 to 5 seconds):* The system maintains a steady speed of 50 rad/s, with the estimated speed matching the reference speed precisely. The measured speed aligns well, with negligible deviation.
- *Acceleration to 150 rad/s (5 to 7 seconds):* The reference speed ramps up to 150 rad/s. The estimated speed tracks this change accurately, though a minor overshoot is observed. The measured speed follows similarly, indicating effective control.
- *Deceleration to 100 rad/s (7 to 10 seconds):* The reference speed reduces to 100 rad/s. Both estimated and measured speeds align closely with the reference, showing quick adaptation to the change.
- *Final Deceleration (10 to 12 seconds):* The reference speed drops to 0 rad/s, and the estimated speed follows promptly. The measured speed also decreases, showing a minor delay but converging to the reference.

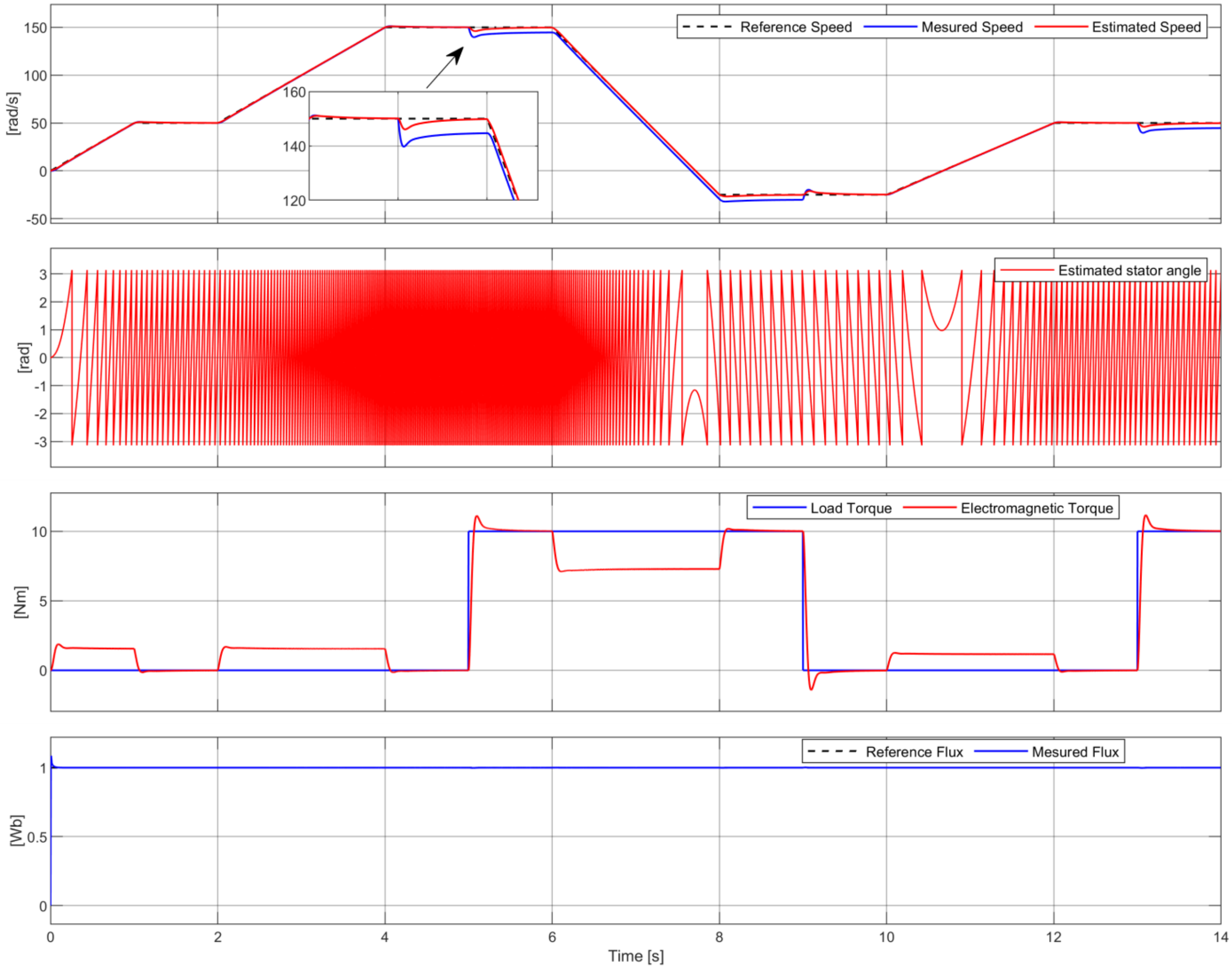

Figure 3. 21: The figure presents the performance analysis of a sensorless control system for an induction motor using the Accurate Adaptive Integration Algorithm. The plots illustrate the following:

1. **Top Plot: Speed response, showing the reference speed (dashed line), measured speed (blue line), and estimated speed (red line).**
2. **Second Plot from Top: Estimated stator angle (red line), demonstrating high-frequency oscillations throughout the operation.**
3. **Third Plot from Top: Torque response, displaying the load torque (blue line) and the electromagnetic torque (red line), with effective tracking of torque changes.**
4. **Bottom Plot: Flux response, showing the reference flux (dashed line) and the measured flux (blue line), with consistent alignment indicating robust flux control.**

Estimated Stator Angle Analysis:

The second plot from the top shows the estimated stator angle (red line). Observations include:

- *High-Frequency Oscillations:* Throughout the entire duration, the estimated stator angle exhibits high-frequency oscillations. These are especially prominent during periods of speed change.
- *Stability*: Despite the oscillations, the angle remains bounded within $[-3,3]$ radians, indicating the system's stability in estimation.

Torque Response Analysis:

The third plot from the top depicts the torque response, where the electromagnetic torque (red line) tracks the load torque (blue line) effectively. Key points are:

- *Initial Torque (0 to 2 seconds):* The load torque is set to 0 Nm, and the electromagnetic torque closely follows this reference.
- *Torque Increase to 5 Nm (2 to 4 seconds):* The load torque increases to 5 Nm, and the electromagnetic torque tracks this change with a slight transient spike, indicating a dynamic response.
- *Steady-State (4 to 6 seconds):* Both load and electromagnetic torque maintain a steady 5 Nm, showing effective control.
- *Torque Decrease and Increase (6 to 12 seconds):* The load torque is varied, showing reductions and increases. The electromagnetic torque accurately tracks these changes, with minor transients indicating good dynamic performance.

Flux Response Analysis:

The bottom plot presents the flux response of the system. Observations include:

- *Reference and Measured Flux:* The reference flux is set at 1 Wb. The measured flux (blue line) aligns very closely with this reference throughout the entire duration, with minimal deviation.
- *Stability:* The consistent tracking of the reference flux by the measured flux indicates robust flux estimation and control.

General Observations

Overall, the sensorless control system exhibits a promising performance. The speed and torque control mechanisms operate effectively, with minor deviations between the estimated and measured values. The high-frequency oscillations in the estimated stator angle, while not compromising overall stability, indicate an area for potential improvement. The stability and accuracy of the system suggest that the Accurate Adaptive Integration Algorithm is a robust solution for sensorless control of induction motors.

Recommendations for Improvement

1. *Noise Reduction:* Implement advanced filtering techniques to minimize noise in the stator angle estimation, thereby reducing high-frequency oscillations.
2. *Algorithm Refinement*: Fine-tune the parameters of the Accurate Adaptive Integration Algorithm to enhance the accuracy of speed and angle estimation.
3. *Transient Response Mitigation:* Investigate methods to smooth transient spikes in torque response for improved dynamic performance.

The results validate the efficacy of the Accurate Adaptive Integration Algorithm in controlling an induction motor without sensors. The close tracking of reference speed, effective torque control, and stable flux estimation highlight the algorithm's strengths. Addressing the identified areas for improvement will further enhance the system's performance, making it a reliable choice for sensorless motor control applications.

3.7 Summary

The aim of this chapter is to present the development procedure of the chosen control algorithm. The analytical discussion in Chapter 1 distinguishes stator field-oriented control (SFOC) as the operating strategy. Therefore, a brief introduction to the concept behind SFOC is provided at the beginning. Following this, the design process begins, focusing on finding the optimal coefficients of PI regulators using two control criteria: magnitude optimum and symmetric optimum. Proper selection ensures system stability, as verified by tests conducted using the MATLAB/SISO tool package.

Additionally, the same theoretical analysis highlights the strong advantages of sensorless control over the use of a rotor position sensor. Consequently, two necessary estimators are introduced: one for stator flux and one for rotor speed. In-depth analysis of potential solutions for flux observation leads to the selection of the optimal method: the accurate adaptive integration algorithm (AAIA) [26]. Even closed-loop SFOC requires precise flux knowledge to execute the strategy effectively, whereas the speed estimator is required solely due to the sensorless demand. A simple velocity observer is designed and tested alongside the entire control algorithm.

Finally, the control strategy is implemented on the system developed in Chapter 2. The system is operated according to the test procedure, and a series of plots demonstrates its overall behavior. Detailed discussion confirms its correctness. However, due to the chosen path, the control algorithm is specifically designed for the conventional motor available in the laboratory. Thus, the presented procedure should be applied and verified when the machine operates at higher frequencies.

Conclusions and Future Work

The main objective of the project is to design a stator field-oriented control algorithm capable of running sensorless and being fully applied in high-speed drives. Due to the unavailability of such motors in university laboratories, the scope was shifted to using a conventional motor supplied with a rated frequency $f_N = 50\ Hz$. To achieve this goal, it is divided into subtasks.

Before laboratory verification of the algorithm, it is essential to check its theoretical performance by simulating it with the modeled system. Therefore, the drive is introduced and validated with the previously mentioned conventional motor. Moreover, the derived motor model can be applied to any asynchronous motor since a set of necessary machine parameters are available. Additionally, the ideal representation of the inverter does not depend on any variables other than those obtained during the simulation. Hence, the entire system can be easily adapted for future verification of the high-frequency drive objective.

To achieve stability in the derived control strategy, the PI controllers need to be properly tuned. This is done using two optimal criteria: magnitude optimum and symmetry optimum. The first criterion is used for parameter selection of the current regulators, while the second one is for tuning the flux and speed controllers. The process yields reliable results, fulfilling design conditions. These results, obtained with simplification applied during the process, confirm the appropriate selection of controller coefficients.

Another crucial aspect of stator field-oriented control is the precise knowledge of the flux magnitude and its position. Several factors determine the necessity for accurate field orientation, further speed estimation, voltage decoupling, or the utilization of a flux regulator. After a brief survey, the appropriate observer is selected and verified in simulation in a closed-loop system running sensorless. The results confirm its correctness, as the estimator tracks the actual flux information accurately. The dependence on speed variation is noticeable; the higher the velocity, the better the performance. To validate the observer, an experiment in the laboratory was conducted, presenting similar behavior to the one obtained from simulation. Consequently, it can be concluded that the flux estimator is designed accurately, with the potential for even better precision at higher speeds.

The second utilized estimator is required by the sensorless demand; thus, the speed estimator is included in the design process. As the objective motor is of an asynchronous type, actual rotational speed depends on two estimations: slip and synchronous velocity. Furthermore, the synchronous speed is derived based on the flux magnitude estimation. Hence, this dependency would amplify errors of previously estimated variables, necessitating the validation of the speed estimator as well. Since the simulation runs sensorless, it can be concluded that the estimator behaves properly. Additionally, a comparison with actual rotational speed is plotted, showing its tracking capabilities. Similarly to the flux observer, the speed estimator's performance was also validated in the laboratory setup, confirming its correctness. Given that speed estimation depends on the flux observer output, it is expected that with increased rotational speed, velocity estimation would improve as well.

Nevertheless, due to time limitations, the main goal of the project could not be fully achieved. All conclusions are based on presumptions. To complete the task, additional tests should be conducted in the future.

Future Work

Several tests and examinations could be included in future work to improve the derived control algorithm:

- Further examination of the designed control strategy: This might involve retuning the PI controllers, and testing with the motor running in a closed-loop, first using an encoder and finally sensorless.
- High-speed machine testing: Since the algorithm is fully validated with a conventional motor, respective tests could be performed with the objective high-speed machine.
- Extended scope on the limitation discussed in Section 1.5:
  - ✓ Analysis of the variation in motor parameters.
  - ✓ Reduction of the stator flux in the field weakening region to extend the speed range.

References

1. Bae, B.-H., et al., *Implementation of sensorless vector control for super-high-speed PMSM of turbo-compressor.* 2003. **39**(3): p. 811-818.
2. Jalili, K., et al. *Design and characteristics of a rotor flux controlled high speed induction motor drive applying two-level and three-level NPC voltage source converters*. in *2005 IEEE 36th Power Electronics Specialists Conference*. 2005. IEEE.
3. Lähteenmäki, J., *Design and voltage supply of high-speed induction machines*. 2002: Helsinki University of Technology.
4. Kennel, R.M. *Ultra high speed drive with permanent magnet synchronous motors and hardware based field oriented control*. in *2007 International Aegean Conference on Electrical Machines and Power Electronics*. 2007. IEEE.
5. Drury, B., *Control techniques drives and controls handbook*. 2001: IET.
6. *High Speed Field Oriented Control*, in *Institute of Energy Technology*. Aalborg.
7. Arkkio, A., T. Jokinen, and E. Lantto. *Induction and permanent-magnet synchronous machines for high-speed applications*. in *2005 International conference on electrical machines and systems*. 2005. IEEE.
8. Xu, L. and C. Wang. *Implementation and experimental investigation of sensorless control schemes for PMSM in super-high variable speed operation*. in *Conference Record of 1998 IEEE Industry Applications Conference. Thirty-Third IAS Annual Meeting (Cat. No. 98CH36242)*. 1998. IEEE.
9. Pellegrino, G., R. Bojoi, and P. Guglielmi. *Performance comparison of sensorless field oriented control techniques for low cost three-phase induction motor drives*. in *2007 IEEE Industry Applications Annual Meeting*. 2007. IEEE.
10. Bojoi, R., P. Guglielmi, and G. Pellegrino. *Sensorless stator field-oriented control for low cost induction motor drives with wide field weakening range*. in *2008 IEEE Industry Applications Society Annual Meeting*. 2008. IEEE.
11. Rees, S. and U. Ammann. *Field-oriented control of current-source inverter fed high speed induction machines using steady-state stator voltages*. in *International Symposium on Power Electronics, Electrical Drives, Automation and Motion, 2006. SPEEDAM 2006.* 2006. IEEE.
12. Kazmierkowski, M.P. and H.J.E.E. Tunia, *Automatic control of converter-fed drives.* 1994. **4**(6).

13. Holtz, J.J.P.o.t.I., *Pulsewidth modulation for electronic power conversion.* 1994. **82**(8): p. 1194-1214.

14. Kaźmierkowski, M.P., R. Krishnan, and F. Blaabjerg, *Control in power electronics: selected problems*. 2002: Academic press.

15. Kazmierkowski, M.P. and L.J.I.T.o.i.e. Malesani, *Current control techniques for three-phase voltage-source PWM converters: A survey.* 1998. **45**(5): p. 691-703.

16. T. L. Andersen, B.S.H., *Field Oriented Control of Saturated Induction Machine*, in *student project*. 2000.

17. Franklin, G., J. Powell, and A.J.I. Emami-Naeini, Upper Saddle River, NJ, *Feedback Control of Dynamic Systems, 5th EditionPearson Education.* 2006.

18. M. Valentini, T.O., A. Raducu, *Control of Variable Speed Variable Pitch Wind*

Turbine With Full Scale Power Converter. student project, 2007.

19. Ogata, K., *Modern Control Engineering*. 4-th edition ed. 2002: Prentice Hall Inc.

20. Umland, J.W. and M.J.I.T.o.I.A. Safiuddin, *Magnitude and symmetric optimum criterion for the design of linear control systems: what is it and how does it compare with the others?* 1990. **26**(3): p. 489-497.

21. Kaliamoorthy, M., S. Himavathi, and A. Muthuramalingam. *DSP based implementation of high performance flux estimators for speed sensorless induction motor drives using TMS320F2812*. in *2006 India International Conference on Power Electronics*. 2006. IEEE.

22. Mihalache, L. *A flux estimator for induction motor drives based on digital EMF integration with pre-and post-high pass filtering*. in *Twentieth Annual IEEE Applied Power Electronics Conference and Exposition, 2005. APEC 2005.* 2005. IEEE.

23. Silveira, A., et al. *A comparative study between tree philosophies of stator flux estimation for induction motor drive*. in *2007 IEEE International Electric Machines & Drives Conference*. 2007. IEEE.

24. Shin, M.-H., et al., *An improved stator flux estimation for speed sensorless stator flux orientation control of induction motors.* 2000. **15**(2): p. 312-318.

25. Jansen, P.L. and R.D.J.I.T.o.I.A. Lorenz, *A physically insightful approach to the design and accuracy assessment of flux observers for field oriented induction machine drives.* 1994. **30**(1): p. 101-110.

26. Zerbo, M., P. Sicard, and A. Ba-Razzouk. *Accurate adaptive integration algorithms for induction machine drive over a wide speed range*. in *IEEE International Conference on Electric Machines and Drives, 2005.* 2005. IEEE.
27. Holtz, J.J.P.o.t.I., *Sensorless control of induction motor drives.* 2002. **90**(8): p. 1359-1394.
28. Munoz-Garcia, A., T. Lipo, and D. Novotny. *A new induction motor open-loop speed control capable of low frequency operation*. in *IAS'97. Conference Record of the 1997 IEEE Industry Applications Conference Thirty-Second IAS Annual Meeting*. 1997. IEEE.
29. Lu, K., *Control Engineering*, in *lecture slides,*. Institute of Energy Technology,

Aalborg University.

Appendix A:

Simulink block diagram in MATLAB for modeling an induction motor

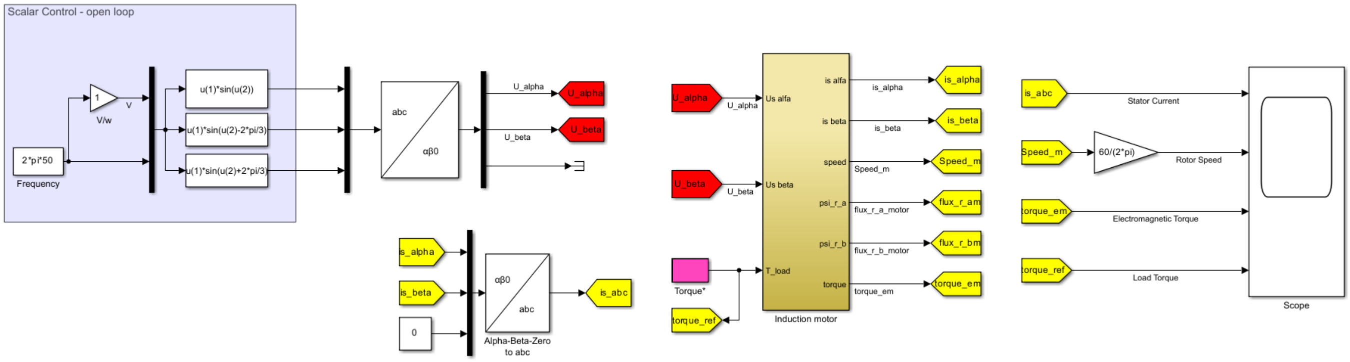

The figure represents a Simulink block diagram in MATLAB for modeling an induction motor using scalar control in an open-loop configuration. Here is a short description:

1. Scalar Control Block (Open Loop):
- This block generates the voltage and frequency reference for the motor, maintaining a constant voltage-to-frequency ratio (V/f control).
2. Voltage Generation:
- The voltage references are modulated as sinusoidal signals for the three phases $\left(u(1) * sin\left(u(2)\right), u(1) * sin(u(2) - 2 * pi/3), u(1) * sin(u(2) + 2 * pi/3)\right)$.
3. abc to αβ Transformation:
- Converts three-phase voltages (abc) to two-phase orthogonal voltages (`αβ`).
4. Induction Motor Block:
- Inputs: Two-phase voltages (U_{alpha}, U_{beta}), load torque (T_{load}).

- Outputs: Stator currents (is_{alpha}, is_{beta}), motor speed $(Speed_m)$, rotor flux components $\left(flux_{r_{a_{motor}}}, flux_{r_{b_{motor}}}\right)$, and electromagnetic torque $(torque_e)$.

5. $\alpha\beta\ to\ abc$ Transformation:
- Converts two-phase currents back to three-phase (abc).
6. Scope:
- Displays various outputs like stator current, rotor speed, electromagnetic torque, and load torque for monitoring and analysis.

This diagram models the dynamics of the induction motor and its response to the applied voltages and load torque.

Appendix B:

Description of the Simulink Block Diagram for Sensorless Control of an Induction Motor Using the Accurate Adaptive Integration Algorithm

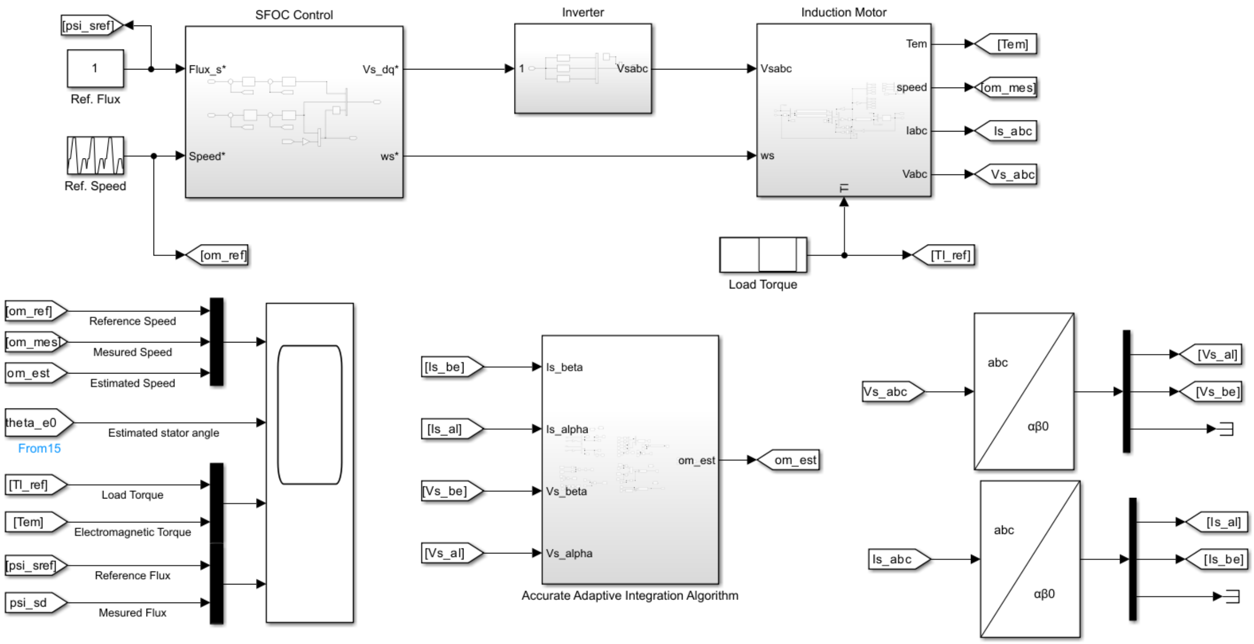

The provided Simulink block diagram illustrates the sensorless control system of an induction motor using the Accurate Adaptive Integration Algorithm. Below is a detailed description of each component and their interactions within the system:

1. *Reference Inputs*

- Ref. Flux ψ_{sref} : This block provides the reference flux value, set to a constant value of 1 Wb.
- Ref. Speed ψ_{sref} : This block provides the reference speed signal, which can vary over time, simulating different operating conditions.

2. SFOC Control Block

- Inputs:
    - Flux referenceFlux_s^*: Reference flux signal.
    - Speed reference Speed^*: Reference speed signal.
- Outputs:
    - V_s^{dq*}: Voltage commands in the dq frame.
    - ω_s^* : Synchronous speed command.

The SFOC (Sensorless Field Oriented Control) block processes the reference inputs and generates appropriate voltage and speed commands for the inverter.

3. Inverter Block

- Inputs:
    - V_s^{abc}: Voltage commands in the abc -frame.
- Outputs:
    - V_s^{abc}: Phase voltages to be applied to the induction motor.

The inverter converts the control signals into the actual phase voltages required to drive the induction motor.

4. Induction Motor Block

- Inputs:
  - V_s^{abc} : Phase voltages from the inverter.
  - ω_s^* : Synchronous speed command.
- Outputs:
  - T_e: Electromagnetic torque.
  - ω_{mes}: Measured speed.
  - I_{abc} : Phase currents.
  - V_{abc}: Phase voltages.

The induction motor block simulates the motor's dynamic behavior based on the applied voltages and load conditions.

5. Load Torque

- Input:
  - $T_{L_{\text{ref}}}$: Reference load torque.

This block simulates the load torque applied to the motor.

6. Accurate Adaptive Integration Algorithm

- Inputs:
  - I_{s_β}: Beta component of the stator current.
  - I_{s_α}: Alpha component of the stator current.
  - V_{s_β}: Beta component of the stator voltage.
  - V_{s_α}: Alpha component of the stator voltage.
- Outputs:
  - ω_{est}: Estimated speed.
  - θ_e: Estimated stator angle.

The Accurate Adaptive Integration Algorithm block estimates the motor speed and stator angle using the inputs provided.

7. Signal Processing Blocks

- Transformation Blocks:
  - $(\alpha\beta)\ to\ (abc)$: Converts signals from the $(\alpha\beta)$ frame to the (abc) frame.
  - $(abc)\ to\ (\alpha\beta)$: Converts signals from the (abc) frame to the $(\alpha\beta)$ frame.
  - Multiplexers: Combine multiple signals for processing or display.

8. Measurement and Feedback

- Measured and Estimated Signals:
  - $(\omega_{\text{ref}}): Referencespeed.$
  - $(\omega_{\text{mes}}): Measuredspeed.$
  - $(\omega_{\text{est}}): Estimatedspeed.$
  - $(\theta_e): Estimatedstatorangle.$
  - $(T_{L_{\text{ref}}}): Loadtorquereference.$
  - $(T_e) **: Electromagnetictorque.$

- (ψ_{sref}): $Referenceflux$.
- (ψ_{sd}): $Measuredflux$.

These signals are used for control, estimation, and monitoring purposes within the system.

The Simulink block diagram represents a comprehensive sensorless control system for an induction motor. The Accurate Adaptive Integration Algorithm plays a crucial role in estimating the motor speed and stator angle, enabling effective control without the need for physical sensors. The system components interact seamlessly to ensure accurate motor control, reflecting advanced control strategies in modern electrical drives.